

## **Copyright Warning & Restrictions**

The copyright law of the United States (Title 17, United States Code) governs the making of photocopies or other reproductions of copyrighted material.

Under certain conditions specified in the law, libraries and archives are authorized to furnish a photocopy or other reproduction. One of these specified conditions is that the photocopy or reproduction is not to be “used for any purpose other than private study, scholarship, or research.” If a user makes a request for, or later uses, a photocopy or reproduction for purposes in excess of “fair use” that user may be liable for copyright infringement,

This institution reserves the right to refuse to accept a copying order if, in its judgment, fulfillment of the order would involve violation of copyright law.

**Please Note: The author retains the copyright while the New Jersey Institute of Technology reserves the right to distribute this thesis or dissertation**

Printing note: If you do not wish to print this page, then select “Pages from: first page # to: last page #” on the print dialog screen

The Van Houten library has removed some of the personal information and all signatures from the approval page and biographical sketches of theses and dissertations in order to protect the identity of NJIT graduates and faculty.

## **ABSTRACT**

### **PASSIVE PLANAR TERAHERTZ RETROREFLECTORS**

**by**  
**Dhruvkumar Desai**

As the application of the Terahertz (THz) band (0.1 – 10 THz) is investigated in various settings, wireless communication stands out as an important frontier to explore. The benefits of increased bandwidth and data rates it promises will only be realized if new technology is developed to support it. Specifically, since THz wireless communication links are typically line-of-sight (LoS), the LoS can be blocked by moving obstacles, thereby requiring alternative link paths. One proposed solution for indoor wireless communications involves systems of steerable antennas, reflective “wallpaper”, and steerable mirrors which would redirect THz beams around a blocking obstacle.

As an initial step in developing steerable mirrors for THz wireless systems, this thesis describes the development of a passive planar terahertz retroreflector based on the Van Atta array. The retroreflector is optimized and simulated using FEM software, fabricated via a low-cost additive manufacturing method, and characterized using terahertz time-domain spectroscopy. Comparison to a flat metal plate shows an increase in monostatic RCS for off-normal angles of incidence.

# **PASSIVE PLANAR TERAHERTZ RETROREFLECTORS**

**by  
Dhruvkumar Desai**

**A Thesis  
Submitted to the Faculty of  
New Jersey Institute of Technology  
in Partial Fulfillment of the Requirements for the Degree of  
Master of Science in Applied Physics**

**Department of Physics**

**August 2018**

Blank Page

**APPROVAL PAGE**

**PASSIVE PLANAR TERAHERTZ RETROREFLECTORS**

**Dhruvkumar Desai**

---

Dr. John F. Federici, Thesis Advisor  
Distinguished Professor of Physics, NJIT

Date

---

Dr. Ian Gatley, Committee Member  
Distinguished Professor of Physics, NJIT

Date

---

Dr. Haim Grebel, Committee Member  
Professor of Electrical and Computer Engineering, NJIT

Date

## BIOGRAPHICAL SKETCH

**Author:** Dhruvkumar Desai

**Degree:** Master of Science

**Date:** August 2018

### **Undergraduate and Graduate Education:**

- Master of Science in Applied Physics,  
New Jersey Institute of Technology, Newark, NJ, 2018
- Bachelor of Science in Physics with Honors,  
United States Military Academy, West Point, NY, 2011

**Major:** Applied Physics

### **Presentations and Publications:**

D. Desai, W. Cole, J. DeLong, and W. Zacherl, "Target Discrimination with a Laser Interrogation," in *Directed Energy Systems Symposium*, Monterey, CA, 2010.

*I have no special talent. I am only passionately curious.*

*– Albert Einstein*

To Ellis, stay curious.



## ACKNOWLEDGMENT

I would like to thank Dr. John Federici for selecting me for this research opportunity and serving as my thesis committee chair. His advice and guidance were instrumental in helping me navigate my journey back into the academic world. With his direction, I have realized my path in life and begun to take those first steps.

Special recognition is reserved for Dr. Ian Gatley for the insights, inspirations, and affirmations received as we investigated this research. We complemented each other well, and it was an honor to pursue this alongside you.

Thank you to Dr. Haim Grebel for providing one of the best classroom experiences I've had and serving on my thesis committee.

I would like to thank my fellow AddLab members Chris Bolton, Lou Rizzo, Carley Mollica, Sam Gatley, and Alex Clark for the engaging conversations, numerous hours of work, and valued friendship throughout my time.

Student support from the DoD Ordnance Technology Consortium (DOTC) DOTC-17-01-INIT0677 program, Topic PAS-17-11 is gratefully acknowledged.

Thank you, Mom, for always pushing us to pursue our education. Despite the long and arduous journeys we endure, nothing compares to the support you have given us during yours.

Thank you to my in-laws for their gracious support and love. Without it, our family could not succeed and thrive.

Finally, an endless amount of love and gratitude to my wife Felicia and son Ellis for their support during this time. Thank you for choosing to join me in this endeavor. We always make hard decisions that force us to escape the comforts of the known, but, in doing so, we face the unknown together.

## TABLE OF CONTENTS

Chapter	Page
1 INTRODUCTION .....	1
1.1 Motivation .....	1
1.1.1 Terahertz in Wireless Communication .....	2
1.1.2 Achieving the Link .....	3
1.2 Objective .....	6
1.3 Background Information .....	7
1.3.1 Retroreflectors .....	7
1.3.2 Van Atta Arrays .....	9
1.3.3 Patch Antennas .....	11
1.3.4 Radar Cross Section .....	13
2 MATERIALS AND METHODS .....	18
2.1 Design .....	18
2.1.1 Antenna Calculations .....	18
2.1.2 Simulation (COMSOL) .....	21
2.1.3 Design Concepts and Ranking.....	25
2.2 Fabrication .....	28
2.2.1 Micro-Dispensing (nScript 3Dn and SmartPump).....	28
2.3 Characterization .....	30
2.3.1 Terahertz Time-Domain Spectroscopy .....	31
2.3.2 Measurement Schemes .....	33

**TABLE OF CONTENTS**  
**(Continued)**

<b>Chapter</b>	<b>Page</b>
3 RESULTS AND DISCUSSION.....	35
3.1 Performance Data.....	35
3.1.1 Flat Plate Measurements.....	35
3.1.2 Co-Polarized Van Atta Measurements.....	39
3.1.3 Cross-Polarized Van Atta Measurements.....	44
3.2 Discussion.....	47
4 CONCLUSION.....	51
4.1 Conclusions and Future Work.....	51
APPENDIX A DESIGN DIMENSIONS.....	53
APPENDIX B MATLAB CODES.....	54
B.1 Antenna Calculations.....	54
B.2 Fast Fourier Transform.....	55
B.3 Time-Domain Data Import Function.....	56
REFERENCES .....	57

## LIST OF TABLES

<b>Table</b>		<b>Page</b>
2.1	Antenna Parameters .....	21
2.2	Design Evolution and Ranking.....	26

## LIST OF FIGURES

<b>Figure</b>	<b>Page</b>
1.1 Terahertz band within the electromagnetic spectrum.....	1
1.2 Smart steerable THz beam system concept.....	6
1.3 Retroreflection.....	7
1.4 Retroreflector examples.....	8
1.5 Van Atta retroreflector concept.....	10
1.6 Possible locations for active components.....	11
1.7 Patch antenna example.....	12
1.8 Radar cross section schematic.....	13
1.9 Normalized flat plate RCS.....	15
2.1 Antenna dimension schematic.....	19
2.2 Example of meshed FEM model.....	22
2.3 Simulation models used.....	24
2.4 Model validation using flat plate RCS.....	25
2.5 Normalized simulated RCS of final design.....	27
2.6 nScript hardware and setup.....	29
2.7 Fabricated samples of Van Atta retroreflector.....	30
2.8 Microscope view of print with dimensions.....	31
2.9 Measurement setup for characterization.....	33
3.1 Frequency response of flat plate.....	36
3.2 Hotspot plot for a flat plate.....	36

**LIST OF FIGURES  
(Continued)**

<b>Chapter</b>	<b>Page</b>
3.3 Normalized total power as a function of angle for a flat plate.....	37
3.4 Normalized power by frequency for a flat plate.....	38
3.5 Averaged normalized power by frequency for a flat plate.....	39
3.6 Frequency response of co-polarized Van Atta retroreflector.....	40
3.7 Hotspot plot for co-polarized Van Atta retroreflector.....	41
3.8 Normalized total power for co-polarized Van Atta retroreflector.....	42
3.9 Normalized power by frequency for co-polarized Van Atta retroreflector..	43
3.10 Averaged normalized power by frequency for co-polarized Van Atta retroreflector.....	43
3.11 Frequency response of cross-polarized Van Atta retroreflector.....	44
3.12 Hotspot plot for cross-polarized Van Atta retroreflector.....	45
3.13 Normalized total power for cross-polarized Van Atta retroreflector.....	46
3.14 Normalized power by frequency for cross-polarized Van Atta retroreflector.....	46
3.15 Averaged normalized power by frequency for cross-polarized Van Atta retroreflector.....	47

# CHAPTER 1

## INTRODUCTION

### 1.1 Motivation

The terahertz band, generally defined by the range of frequencies from 0.1 – 10 THz, occupies an interesting portion of the electromagnetic spectrum [1]. Shown in Figure 1.1, this region's position between the electronics and photonics realms highlights its potential for application in areas dominated by the latter two, lending itself subject to similar properties as well [2].



**Figure 1.1** Terahertz band within the electromagnetic spectrum.

Source: Fujitsu, "Relationship between electromagnetic wavelengths and frequencies," 20110912-01a\_tcm100-930360.jpg, ed. Kawasaki, Japan, 2011.

While once largely unexplored, the “terahertz gap”, to which it is commonly referred, has been coming into the light [4]. As evidenced by the increase in publications and presence of devoted technical sessions by major societies, the emergence of THz applications was driven by research in defense and material science [5]. Other uses have since expanded to security, medicine, biology, space, and manufacturing [1] [6]. Now, one of the latest areas to explore the THz potential is wireless communication.

### **1.1.1 Terahertz in Wireless Communication**

Edholm's Law describes the rate of increase of bandwidth in telecommunications as the years progress. Like Moore's Law, Phil Edholm predicted that data rates from both wired and wireless communications will continue double every 18 months [7]. This corresponds to rates up to 10 Gbps by the next few years, a striking million-fold rise from the 1980s, with wireless data rates potentially approaching 1 Tbps [4]. Additionally, a great influx of users and devices has begun to crowd the space, as much of the communication has been regulated to bands below 5 GHz [6]. In a recent IP traffic forecast, Cisco estimated that Internet traffic would increase nearly threefold in the next five years, to over three Zettabytes (three billion Gigabytes) per year by the end of 2021 [8]. This staggering amount of data, which continues to grow, demands new schemes to exchange information. Finally, we are beginning to address the possibility of a new spectral range for wireless communications. The THz band has within it the potential to deliver high speeds and increased capacity, making it a viable next step.

In 2007, progress toward this step was made evident when IEEE 802.15 Working Group on Wireless Personal Area Networks (WPAN) formed the Interest Group on Terahertz to explore the potential uses in communication [9]. Benefits of using the terahertz band include the following:

1. The available bandwidth is significantly greater than that in the microwave and mm-wave regions [1] [4].
2. Data rates around 1 Tbps are possible, which are unattainable below 0.1 THz. Optical frequencies can reach these speeds but are constrained by the complexity and size of required equipment [4].
3. There is a lower attenuation in adverse weather versus the optical band [1].



4. Diffraction is also reduced compared to microwaves, which allows for a more secure link [4].
5. Aside from a few portions used for radio astronomy and remote sensing, much of the band remains unregulated [10].

One limitation to the maximum wireless link distance for outdoor communications is atmospheric path loss [6] [11]. Despite the advantages of THz wireless links over optical wireless links in bad weather conditions such as fog, there remain wide swaths of THz frequencies that are severely attenuated in common atmospheric conditions [1]. While there has been some concern (Piesiewicz et.al.) that high attenuation of certain THz frequencies may restrict outdoor use of THz links to low-moisture, stable weather locations and limit the use of the THz band to indoor links of short/medium range [12], it is possible to utilize the low-attenuation atmospheric “windows” for an outdoor THz system. For example, THz links of 100 Gbps over short distances have been demonstrated [13]. A long distance 21km link operating at 0.14 THz with a data rate of 5Gbps has been demonstrated [14]. However, it is an ongoing initiative to develop supporting technology such as sources, modulators, detectors, etc. for a THz wireless system. The lack of advanced THz components and subsystems is limiting progress [1] [4].

### **1.1.2 Achieving the Link**

In [6], analysis of the Friis transmission formula emphasizes the directional nature of THz radiation. The formula is commonly written as the following

$$\frac{P_r}{P_t} = e_r e_t \left( \frac{\lambda}{4\pi R} \right)^2 D_r D_t \quad (1.1)$$

where  $r$  and  $t$  represent the receiver and transmitter, respectively,  $P$  is the power,  $e$  is the antenna efficiency,  $\lambda$  is the free-space wavelength,  $R$  is the distance between the receiver and transmitter, and  $D$  is the directivity [15].

Clearly, as is it written, the received power is dependent on the square of the wavelength, which argues against the use of higher frequencies for communications. But looking closer at the directivity, it is shown that the effects of diffraction can be applied to reintroduce a wavelength dependence, only this time in an inverse square relationship [15]:

$$D = \frac{4\pi A^2}{\lambda^2} \quad (1.2)$$

$$\frac{P_r}{P_t} = \frac{A_r A_t}{\lambda^2 R^2} \quad (1.3)$$

$A$  is the effective area of the antenna. Now, one can see that diffraction in the far-field allows for a narrower beam in the THz frequencies.

Because of this directionality, THz communications will be inherently line-of-sight (LoS) based. For certain scenarios, such as outdoor wireless links between buildings, this is virtually no issue. Widespread use, however, will prove to be problematic when blockages can occur [6]. In the 5G concept presented in [16], THz transmitters could be utilized to provide high-speed connectivity to mobile

users. The essential freedom of maneuver provided by mobile receivers means that obstacles to the signal are inevitable. For indoor situations, furniture and even other people can block transmission. Outdoors, a walking receiver can lose the signal.

This non-line-of-sight (NLoS) communication will require new technology that can maintain the link between transmitters and receivers. A “smart” steerable antenna system [2] [6] consisting of steerable antennas, reflective wall paper, and reflective relays (i.e. electronically steerable mirrors) has been identified [6] [17] as one of the key components which needs to be developed for indoor THz communication systems. Antenna arrays would be indispensable in the THz range due to the need for automatic accurate beam forming/switching to compensate for LoS loss experienced in this environment due to moving obstacles (humans) or wireless devices. Electronically steerable mirrors could function as relays in the case of a LoS loss.

One commonly presented solution for reflecting THz beams to compensate for LoS loss is reflective “wallpaper”. Some well-known developments in the latter involve dielectric mirrors that rely on alternating indices of refraction to reflect THz radiation [18] [19]. Steerable antennas, as conceptualized in [16], would require some sort of mirror as well. The longer term goal of this research direction is to develop an electronically steerable planar mirror which can relay a THz beam to alternative link paths as illustrated in Figure 1.2.

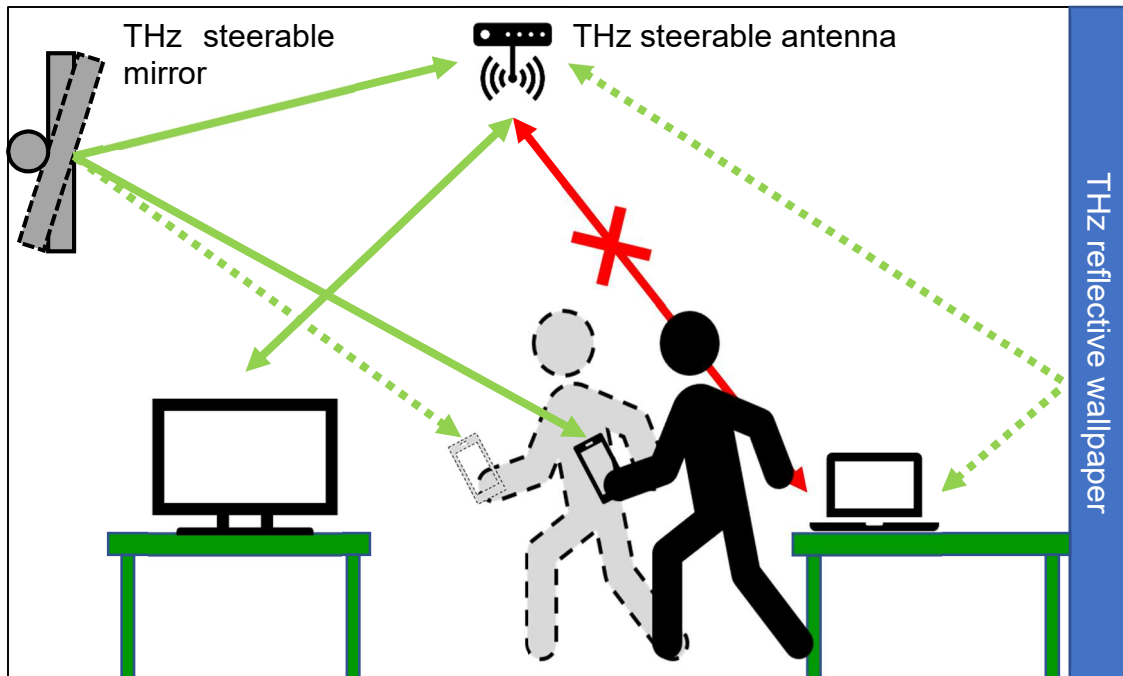


**Figure 1.2** Smart steerable THz beam system concept. A steerable antenna directs the THz data link to the client devices. An obstructed link is redirected via reflective wallpaper. A moving client device’s link is maintained by a steerable mirror.

## 1.2 Objective

In this thesis, a new approach to the THz mirror design is investigated: Van Atta array reflectors. As described in Section 1.1.2, phase shifters can be integrated into the Van Atta design enabling an electronically steerable mirror which could potentially enable the smart steerable beam system illustrated in Figure 1.2. As an initial step in the development of Van Atta arrays in the THz, the objective of this thesis is to design, fabricate, and characterize a passive planar retroreflector for the terahertz frequencies. Using examples and guidelines from literature, designs will be developed and optimized using finite-element method software (COMSOL). Designs will be ranked by simulated performance and the selected model will be

fabricated using micro-dispensing hardware (nScript SmartPump). Finally, the simulations will be validated using a terahertz time-domain spectroscopy tool (T-Ray 2000).

## 1.3 Background Information

### 1.3.1 Retroreflectors

Retroreflection is the phenomenon by which electromagnetic radiation is reflected back towards the source [20]. As opposed to planar mirrors, this can occur for angles of incidence ( $\theta$ ) other than boresight, as shown in Figure 1.3 below. This property lends itself to many practical uses, both everyday and technical.

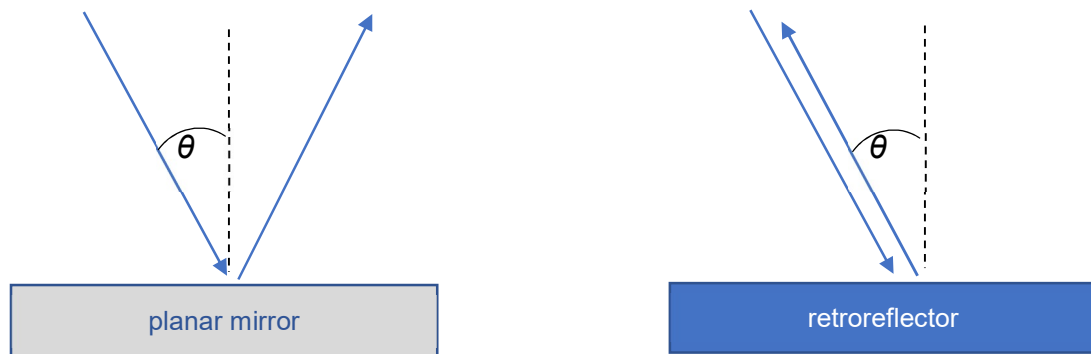


**Figure 1.3** Specular reflection from a planar mirror (left) and retroreflection back towards source (right).



**Figure 1.4** Examples of common retroreflectors in road signs and bicycles (left) and Lunar Laser Ranging Retroreflector on the moon (right)

Sources: Lucent, Glowing-retroreflector-web.jpg, ed: Lucent Optics, 2018.

S. Rowe, "Retroreflectors: Common uses, uncommon applications and the Lunar Laser Ranging Experiment," ed. Oak Ridge, NJ: Esco Optics, 2017.

Many safety-oriented products such as bicycles and clothing have retroreflective materials embedded to aid in detection during low visibility conditions. Retroreflectors have been used by NASA to measure the Earth-Moon separation and by other researchers in optical detection [20] [23].

In [24], common types of passive retroreflectors are analyzed. These include dihedral and trihedral corner reflectors (flat reflective surfaces joined orthogonally into a 3D structure) and the Luneberg lens (a sphere of dielectric

material with a radially-dependent relative permittivity and a metallic cap). When examining their performance over varying angles of incidence, both offer a significant improvement off-normal but fall short of the third type of retroreflector examined in [24], the Van Atta array.

### **1.3.2 Van Atta Arrays**

In 1959, Lester C. Van Atta was awarded a patent for an “electromagnetic reflector” which was designed to be “an array of antennas for reflecting an incident electromagnetic wave back in a predetermined direction that is capable of operating at wide angles of incidence” [25]. These arrays consist of antennas connected in pairs that will retroreflect incident radiation. For proper operation, the antennas within each pair must be diametrically opposed about the center and connected by transmission lines of equal electrical length (integer multiples of the wavelength). By doing this, the emitted radiation, even from different pairs, align in phase. The original concept, using horn antenna as an example, is shown in Figure 1.5. The arrival of the wavefront at an angle  $\theta$  causes a phase delay in the rays incident on the antennas. Since the pairs connected are opposite one another about the center, the phase delay in any receiving antenna is offset by that in its paired transmitting antenna and vice versa [26].

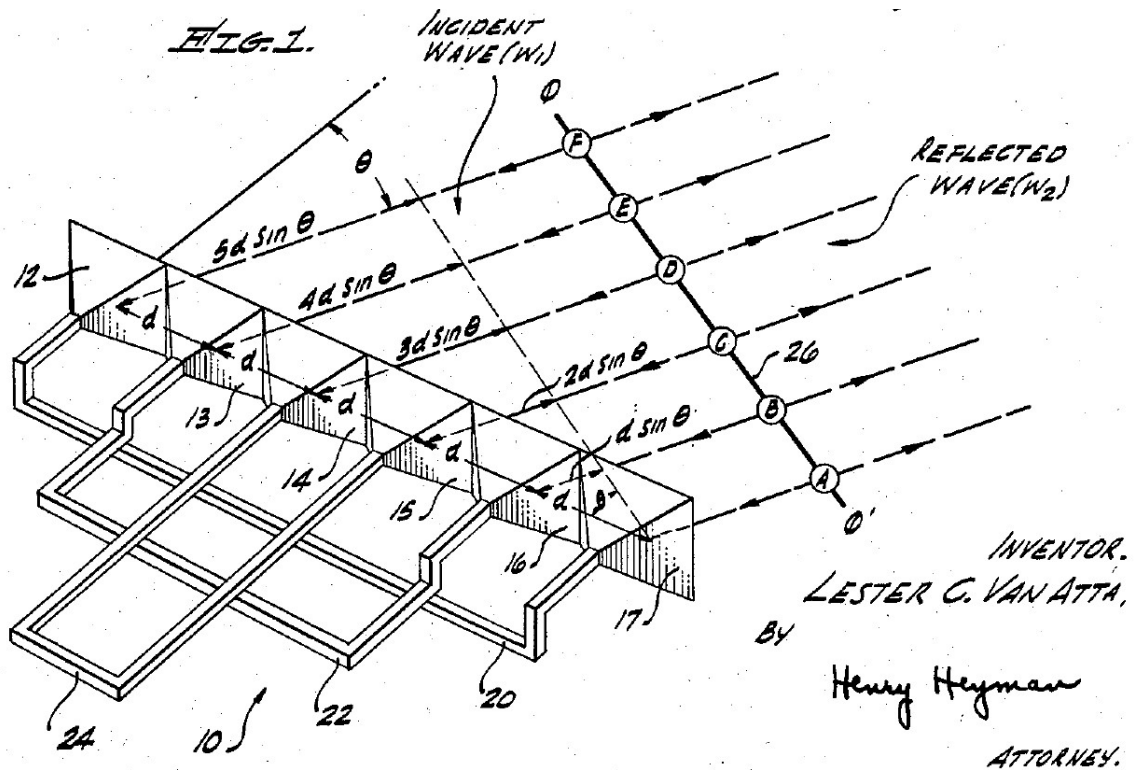


**Figure 1.5** Retroreflector concept proposed by Van Atta. Incident rays reflect back towards the source in phase. This is made possible by transmission lines that are equal in electrical length connecting pairs of antennas that are diametrically opposed.

Source: L. C. Van Atta, "Electromagnetic Reflector," US Patent 2,908,002, October 6, 1959.

The comparison done in [24] showed that the Van Atta array had a broader return signal versus angles of incidence compared to the corner reflector and Luneberg lens. In addition, for a comparable radar cross section, the Van Atta array would be smaller and significantly thinner than both. Though the latter two are better equipped to operate over a wider bandwidth, the design of Van Atta array makes it ideal for operation within a specific band, as would be necessary for wireless communications. The choice of antenna allows the array to operate at specific frequencies. Moreover, there is potential to include electric switching and amplifying capabilities within the Van Atta structures, shown in



Figure 1.6 suggesting a promising approach to developing Van Atta structures as ‘smart’ steerable mirrors [24]. These would be integrated into a “smart” antenna system for THz wireless communications, such as one illustrated in Figure 1.2.

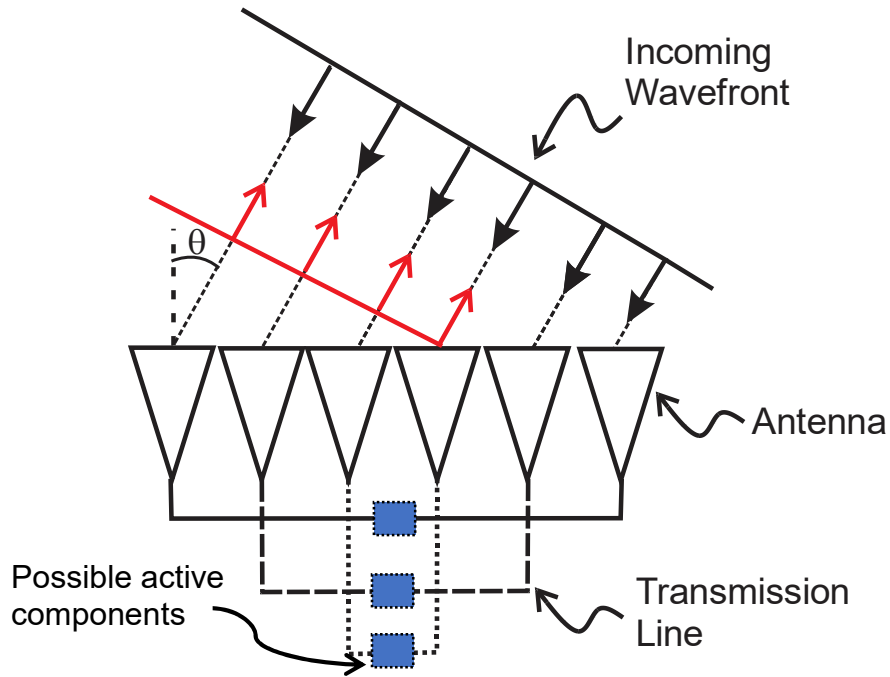


**Figure 1.6** Van Atta array diagram showing possible locations for active components. These can include amplifiers and/or phase delays.

An important consideration in the Van Atta design as compared to the alternative 3D retroreflecting structures described in [24] is that the Van Atta arrays can be printed using additive manufacturing methods into a 2D planar structure.

### 1.3.3 Patch Antennas

To meet the objective, we must choose a relatively thin antenna. None is better suited for this task than the microstrip antenna. In its simplest form, it consists of a conductive “patch” on a dielectric layer followed by a ground plane. Popularized in

the 1970s, this versatile antenna, depicted in Figure 1.7, holds many advantages suitable for this application [27]:

1. They can be fabricated easily.
2. They are easily integrated into circuits and arrays for enhanced performance.
3. By design, they are thin and even flexible.
4. There are varied approaches to feeding, each of which can be advantageous for improving losses, directivity, or impedance matching.



**Figure 1.7** Example of inset-fed patch antenna with a microstrip feed line.

Source: Saturn PCB, "915MHz Patch Antenna," 915MHz\_Patch\_Antenna-big.png, ed. Orlando, FL: Saturn PCB Design, Inc., 2017.

Sacrifices that must be made for their ease of use include low bandwidth and decreased efficiency and power [27]. These can be overcome by choice of parameters during design and arraying. These design considerations will be discussed later.

### 1.3.4 Radar Cross Section

Once a proposed design for the retroreflector is chosen, comparisons must be made to determine its performance relative to other solutions. A common approach is to look at the radar cross section (RCS). Though initially used to describe scattered energy from a target back to a receiving radar, this term is more general in practice and readily implemented in other frequencies as well [29].

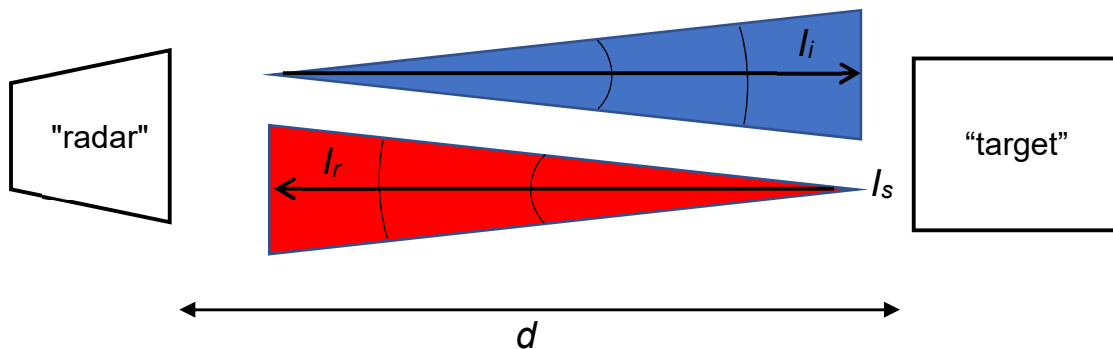


**Figure 1.8** Determination of the radar cross section of a “target”. RCS is proportional to the ratio of scattered intensity (at the radar after divergence) to incident intensity (at the target).

To determine the value, we consider one “radar” (which serves as both the transmitter and receiver for *monostatic RCS*) and a “target”, as depicted in Figure 1.8. The RCS of an object ( $\sigma$ ) effectively reduces the incident energy. Following the similar derivation in [29], if  $I_i$ ,  $I_s$ , and  $I_r$  represent the incident, scattered, and return intensities, respectively:

$$I_s = \sigma I_i \quad (1.4)$$

This scattered intensity, however, is not what returns to the radar. It is further reduced due to the inverse-square law [30] as it travels back over the separation distance,  $d$ .

$$I_r = \frac{I_s}{4\pi d^2} \quad (1.5)$$

Substituting and solving for the RCS value:

$$\sigma = \frac{I_s}{I_i} = 4\pi d \frac{I_r}{I_i} \quad (1.6)$$

These measurements are usually taken in the far-field, where the separation distance much greater than the wavelength, which allows for the plane wave approximation to hold [29]. Thus, a small change is needed:

$$\sigma = \lim_{d \rightarrow \infty} 4\pi d^2 \frac{I_r}{I_i} \quad (1.7)$$

For the study of a retroreflector, it is important to consider the angle of incidence of the directed energy. Though not explicitly seen in Equation 1.7, the RCS of any object (placed at the origin of a spherical coordinate system) will be a function of the polar ( $\theta$ ) and azimuthal ( $\phi$ ) angles, as well as the distance to the source,  $d$ . One of the challenges to the implementation of THz wireless

communications was the need for NLoS links, which could occur at random angles depending on the locations of the transmitters and/or receivers. In order to remain effective, a THz retroreflector must be able to operate well over a relatively broad range of angles.

In the case of the flat metal plate, a strong specular reflection is the source of most of its RCS value. As the angle of incidence shift from normal, the RCS steeply drops as seen in Figure 1.9.

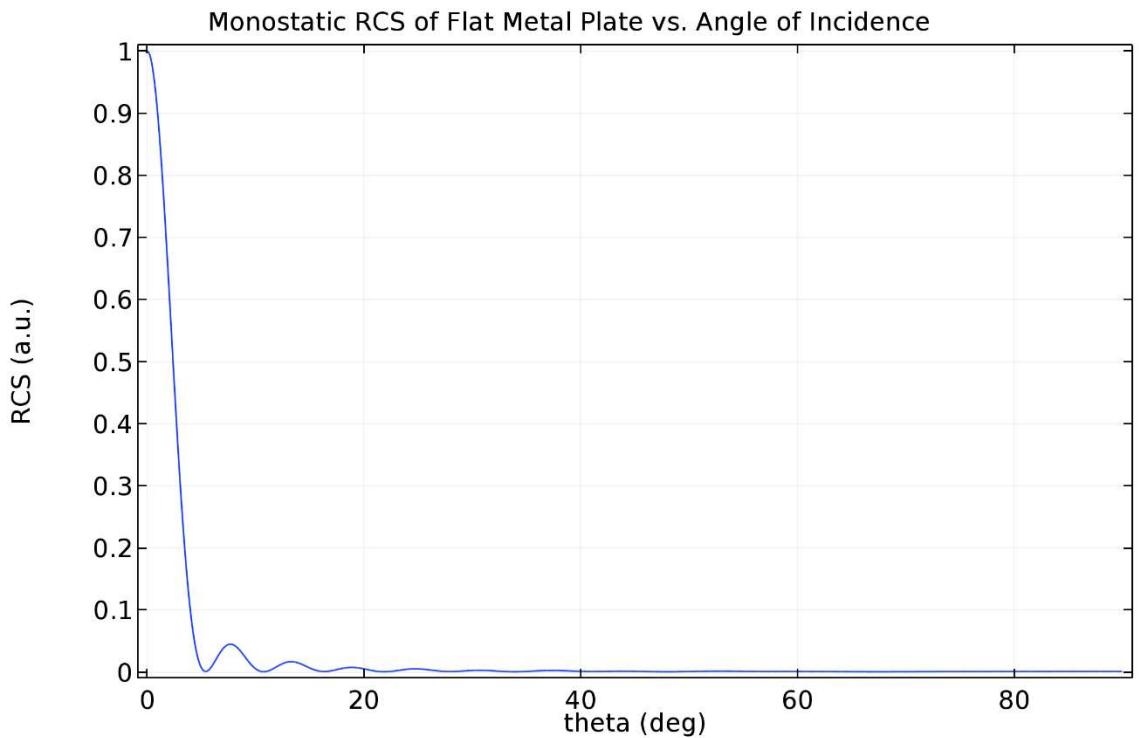


**Figure 1.9** Normalized monostatic RCS of flat metal plate.

For the study at hand, it is necessary to further define a figure of merit to rank the performance of concepts during the design phase. While RCS values over angles of incidence will depict an accurate representation of the performance over angles, a *rotationally-averaged* RCS will provide a single value to quantify the

overall performance of the retroreflectors. This can be calculated by taking the surface average of the monostatic RCS.

$$\sigma_{r.a.} = \frac{1}{N} \iint_S \sigma_m(r = d, \theta, \varphi) dS \quad (1.8)$$

Because only the behavior of the waves in front the retroreflector is considered, the integral is restricted to first four octants, where  $\theta$  ranges from 0 to  $\pi/2$ , on a ball of radius  $d$ , the distance between the source and the sample.  $N$  is a normalization constant determined by the bounds.

$$\sigma_{r.a.} = \frac{1}{2\pi} \int_0^{2\pi} \int_0^{\frac{\pi}{2}} \sigma_m(r = d, \theta, \varphi) \sin \theta d\theta d\varphi \quad (1.9)$$

With an analytic form for  $\sigma_m$ , Equation 1.9 would provide an excellent metric for ranking performance of retroreflector design. Obviously, this is not feasible, and thus approximation is necessary.

$$\sigma_{r.a.} \approx \frac{1}{2\pi} \sum_i \sum_j \sigma_m(r = d, \theta_i, \varphi_j) \sin \theta_i (\Delta\theta)(\Delta\varphi) \quad (1.10)$$

The double integral is converted to a double sum over discrete values of  $\theta$  and  $\varphi$ .  
As will be discussed later, finite-element method software calculates  $\sigma_m$  to easily  
determine  $\sigma_{r.a.}$

## CHAPTER 2

### MATERIALS AND METHODS

#### 2.1 Design

Using guidelines and examples from literature, the Van Atta array of patch antennas was conceptualized and modeled in COMSOL, a commercially available simulation software. The model was vetted using the known solution of the flat plate. Designs were ranked by their rotationally-averaged RCS and the best performing design was fabricated.

##### 2.1.1 Antenna Calculations

The key to proper operation is achieving resonance. Microstrip antennas are commonly referred to as “half-wave patches” because their resonant size is one-half of a guided wavelength.

$$L_{eff} = \frac{\lambda_g}{2} = \frac{\lambda_0}{2\sqrt{\epsilon_{r,eff}}} = \frac{c}{2f\sqrt{\epsilon_{r,eff}}} \quad (2.1)$$

The  $L$  corresponds to the length of the patch. The purpose of the *eff* subscript is illustrated in Figure 2.1.



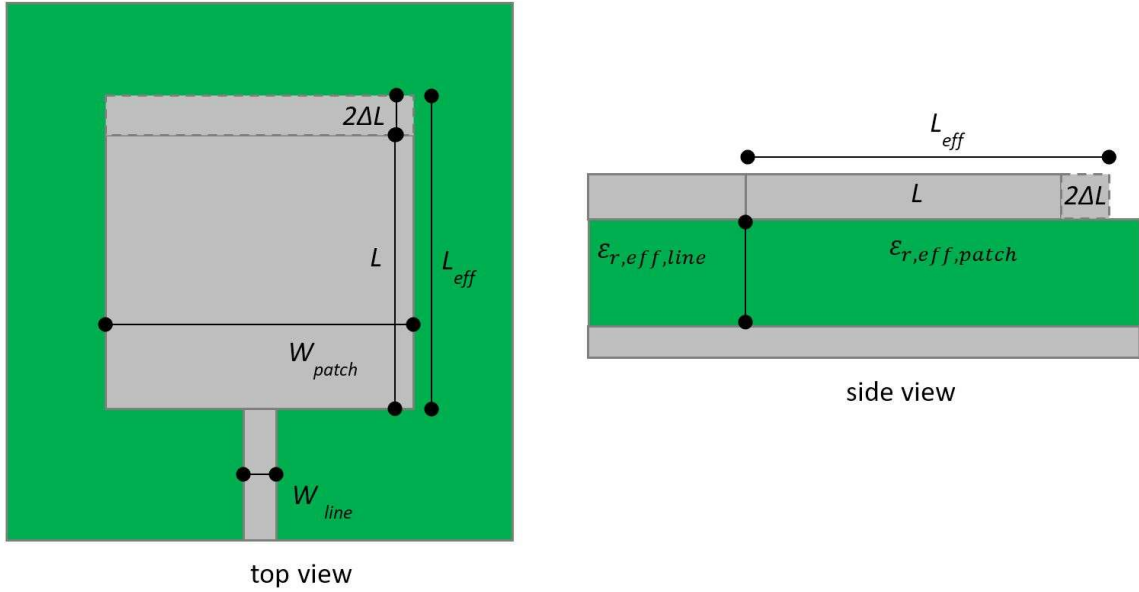


**Figure 2.1** Schematic of antenna dimension. Due to effect of fringing fields, patches seem longer in terms of resonance. Different widths induce an effective dielectric constant.

Due to the fringing fields at the edge of the microstrip (both the patch and transmission line), there is a necessary correction to the calculations, which takes the form of an effective dielectric constant [31]. This is dependent on the width  $W$  and the height of the microstrip above the ground plane,  $h$ , which is the thickness of the dielectric material.

$$W = \frac{c}{2f \sqrt{\frac{\epsilon_{r,eff} + 1}{2}}} \quad (2.2)$$

$$\epsilon_{r,eff} = \frac{\epsilon_r + 1}{2} + \frac{\epsilon_r - 1}{2} \left( \frac{1}{\sqrt{1 + \frac{12h}{W}}} \right) \quad (2.3)$$

Note that the two parameters in Equations 2.2 and 2.3 are mutually dependent. Therefore, an iteration scheme is needed to converge to a solution. Also, since this effect will occur on both the lines and the antenna, there will be a corresponding  $\epsilon_{r,eff}$  for each. This is especially important because the guided wavelength  $\lambda_g$  will differ in the two regions.

As seen in Figure 2.1, the desired length of the patch  $L$  is augmented by  $\Delta L$ . This is another correction factor needed to identify the proper resonant parameter. As the wave approaches the patch from the transmission line, there may be a step up in width, but the field lines can continue along the patch. When it hits the end of the patch, there is no more conductive material and the field lines fringe here as well. This is known as an open end, and  $\Delta L$  is the corresponding correction [32].

$$\Delta L = 0.412 h \frac{(\epsilon_{r,eff} + 0.3) \left(\frac{W}{h} + 0.264\right)}{(\epsilon_{r,eff} - 0.258) \left(\frac{W}{h} + 0.8\right)} \quad (2.4)$$

$$L = L_{eff} - 2\Delta L \quad (2.5)$$

Beginning with a design frequency of 0.2 THz (200 GHz), the calculated parameters for the antenna and transmission lines are given in Table 2.1 below. Some parameters are fixed due to a priori knowledge of material properties and printing capabilities. This also simplified the design process by reducing the

degrees of freedom during simulation. If square patches are needed, the iteration will include length calculations and resetting the width to equal the final length. The MATLAB code is available in Appendix B.

**Table 2.1** Antenna Parameters

Parameter	Description	Value
$f$	Resonant frequency	200 GHz*
$h$	Thickness of substrate	52 $\mu\text{m}^*$
$\epsilon_r$	Dielectric constant of substrate	3.6*
$\epsilon_{r,eff,line}$	Dielectric constant under trans line	2.76
$\epsilon_{r,eff,patch}$	Dielectric constant under patch	3.10
$W_{line}$	Width of trans line (based on print)	90 $\mu\text{m}^*$
$W_{patch}$	Width of patch (set equal to $L$ )	377.9 $\mu\text{m}^*$
$L_{eff}$	Effective length of patch (also $0.5 \lambda_g$ )	425.8 $\mu\text{m}$
$\Delta L$	Open end length correction to patch	23.9 $\mu\text{m}$
$L$	Actual length of patch	377.9 $\mu\text{m}$
$\lambda_{g,line}$	Guided wavelength along trans line	851.6 $\mu\text{m}$

\* fixed parameters

### 2.1.2 Simulation (COMSOL)

Obviously, developing and testing different design concepts for a Van Atta retroreflector can be tedious. A simulation software is well-suited for this type of problem. One is able to set and tweak parameters and quantify performance without fabrication and testing, which can be costly and time-consuming. The specific software used in this study is COMSOL and its RF Module.

COMSOL is a finite element method (FEM) simulation software. For many electromagnetic problems, the key to a solution is solving Maxwell's equations at all points. Clearly, this is not physically possible. Instead, numerical approximations are made. FEM is one such approximation to solving ODEs and PDEs with difficult or no analytical solutions. Once a model is built or imported into

a study, a mesh is generate using small customizable elements. The locations of the vertices of these connected finite elements are known as nodes, and that is where the approximations are taken [33]. The smaller the mesh element size, the more accurate the approximation – but with a significant computational power cost. When creating a model, it is crucial to mesh *sufficiently* rather than intensely, for there can be just as accurate solutions found with coarser (and thus faster) meshes. For electromagnetics, it is commonly accepted to set the largest mesh element smaller than  $\lambda_0/5$ . Figure 2.2 depicts the meshing used in the final design.

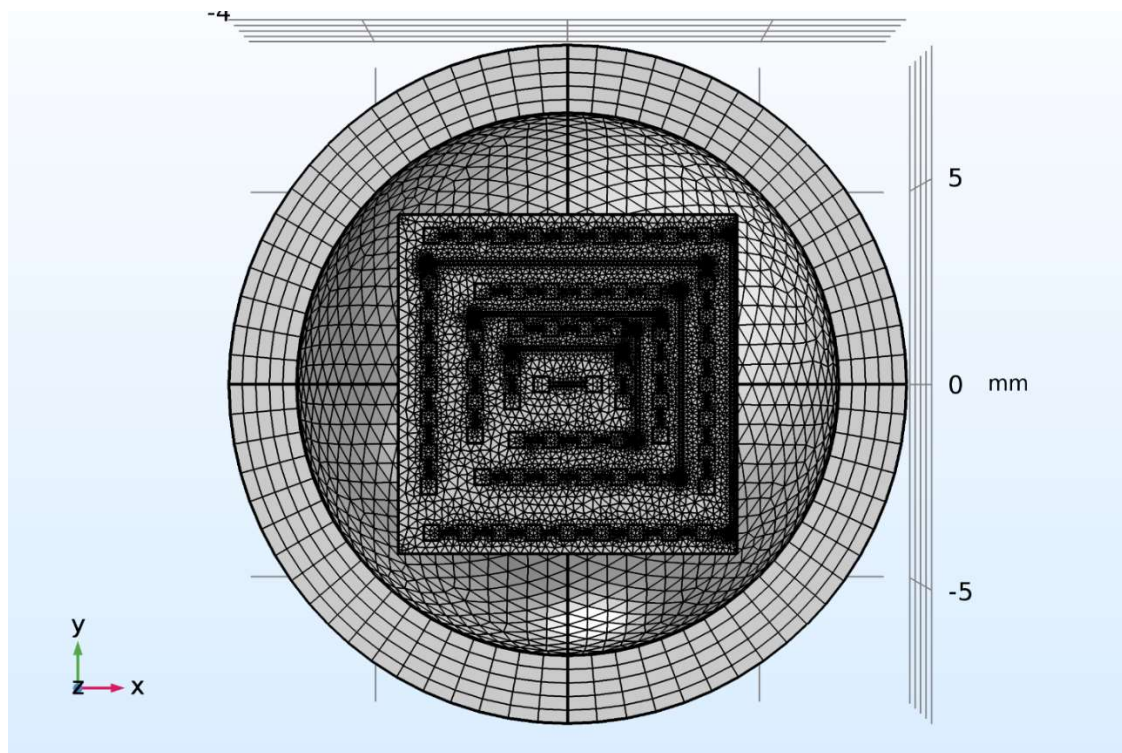


**Figure 2.2** Meshed model of Van Atta array depicting dense element concentration on the structure itself. Physically small areas, such as the transmission lines and bends, have significantly more mesh elements.

The RF Module within COMSOL uses a full wave formulation when solving for the electric field. This term refers to use of the full time-dependent Maxwell's equations to solve problems where structures are electrically comparable to the wavelength in question [34]. This differs from quasi-static cases, where propagation of the wave does not affect the conditions over a reasonable time period. The Far Field Domain node is most applicable to this study. Without having to model large distances, it uses the Stratton-Chu formula which accounts for the distance from the antenna to the field point and the solution of the near-field electric field and ignores the background (or incident) field. This scattered field is then used to calculate the bistatic RCS.

To accommodate the study here, it was more efficient to modify existing models that were included as examples and tutorials rather than building a new one. In particular, "radar\_cross\_section.mph", "rsc\_sphere.mph", and "microstrip\_patch\_antenna\_inset .mph" (shown in Figure 2.3a-c) were modified. Monostatic RCS is not calculated by COMSOL organically. Thus, the 2D model calculates the monostatic RCS of an object using a coordinate mapping function on the bistatic RCS solution. The 3D RCS model had the appropriate node and study structure that would accommodate the Van Atta array. Finally, the antenna model is used to validate the parameters calculated and study effects of frequency shifts and impedance matching. A combination of all three is the final simulation base for this thesis, shown in Figure 2.3d.

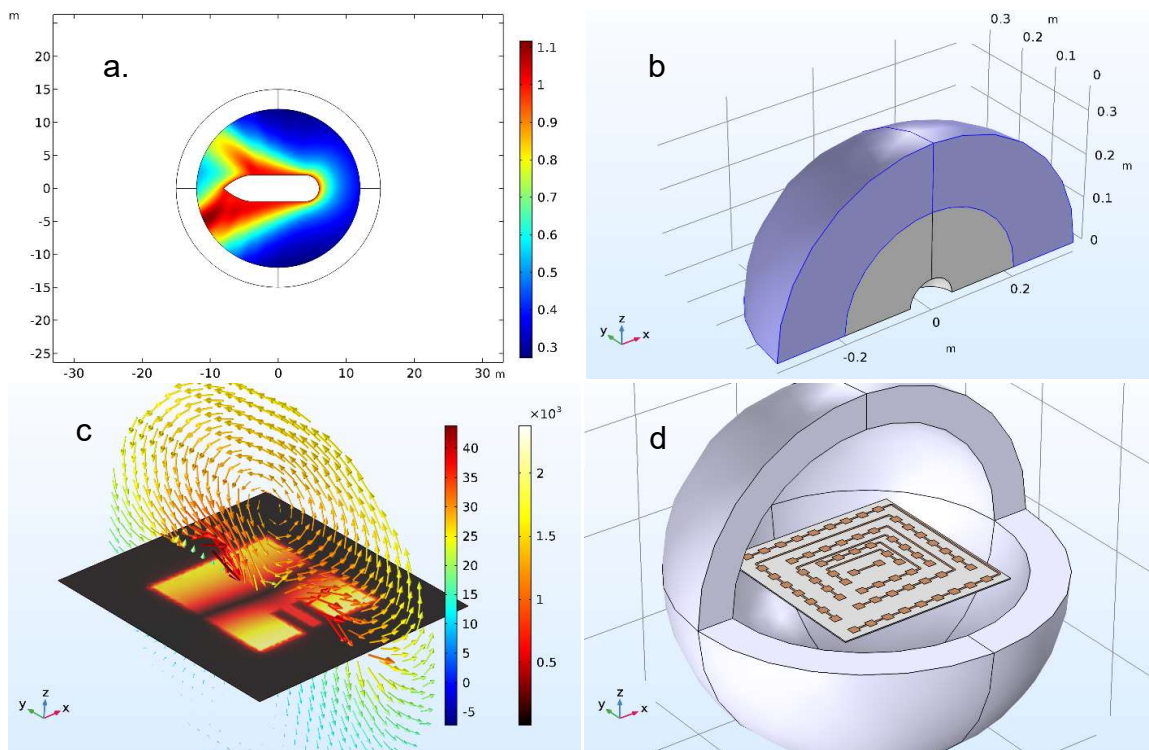


**Figure 2.3 a.-c.** Pre-existing models used to create base simulation for this thesis, shown in **d**. The spherical shell is the “perfectly matched layer”, a non-physical simulation construct that aids in the study of the far-field domain by absorbing spurious reflections.

Once the simulation was configured to deliver the desired solution, it had to be validated. A solution for the RCS of a flat metal plate is very well-known and serves as a litmus test [35]. Similar to Fraunhofer diffraction [30], the analytic form of the RCS of a flat rectangular plate can be determined using the spatial Fourier transform of the aperture function and a plane wave with a varying angle of incidence. The result is the square of a sinc function with a maximum at  $\theta = 0$ . Running the simulation to solve for the monostatic RCS and comparing the result

to that of the flat metal plate, it is easy to see that the model coincides well with theory. This validation is crucial for the design process, as much time and effort can be wasted on running simulations that are not accurately representing the physical phenomena.

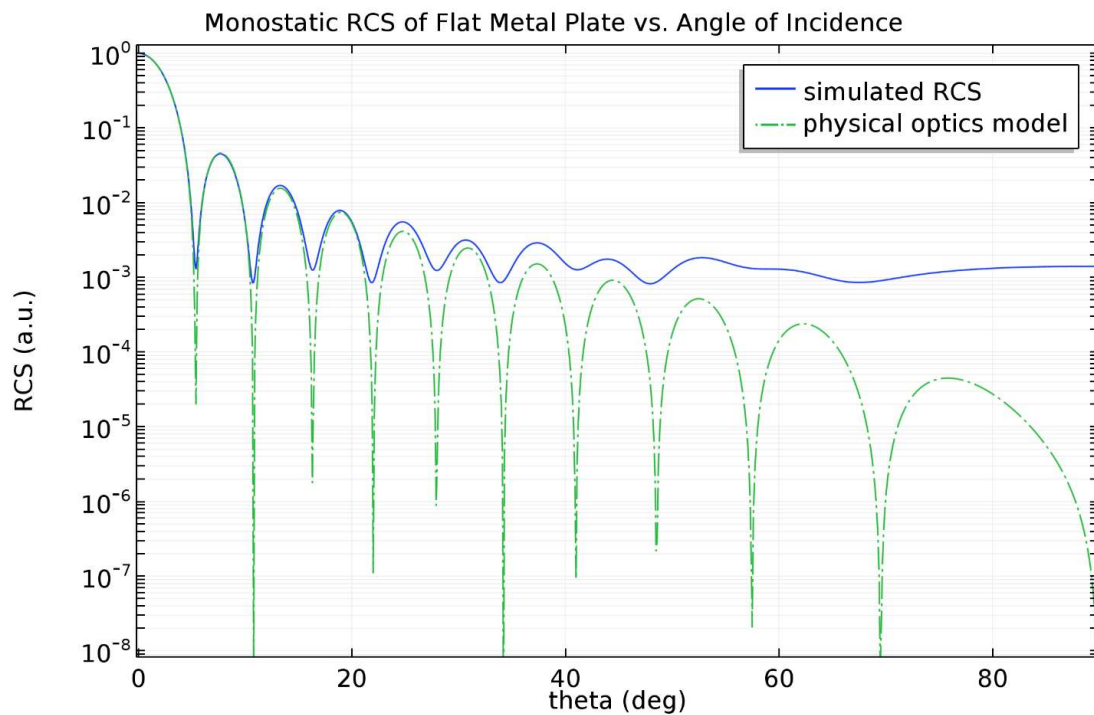


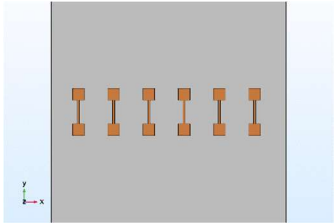
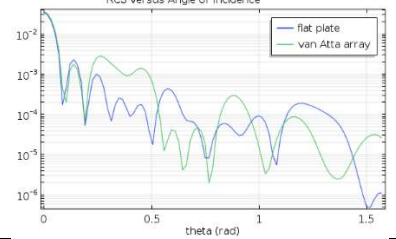
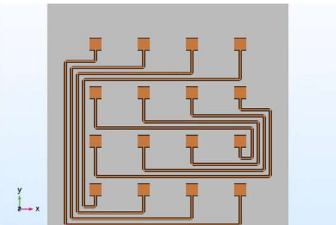
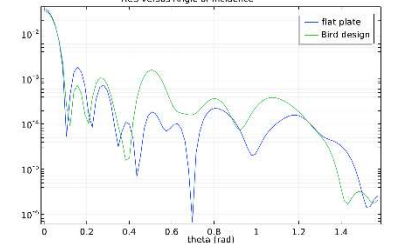
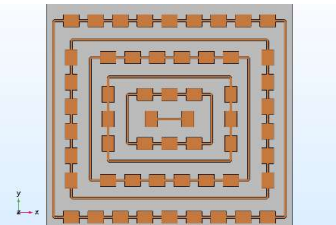
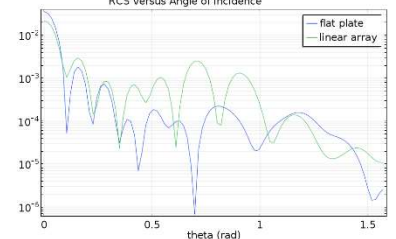
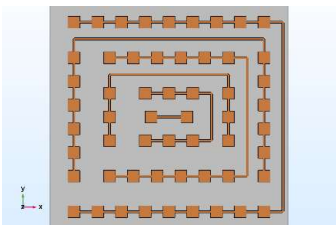
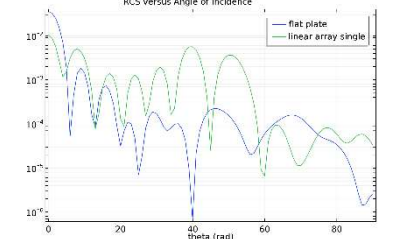
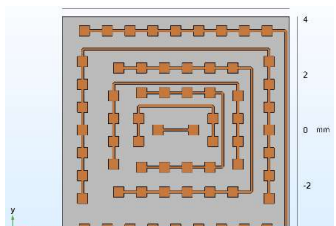
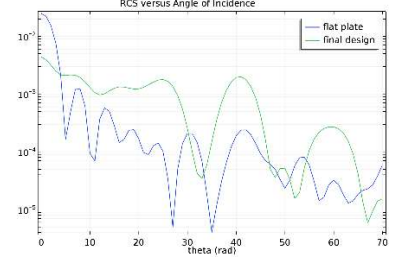
**Figure 2.4** COMSOL model delivers results that are validated using the analytic solution to the flat metal plate. The divergence of the two solutions at shallower angles can be attributed to corrections necessary for the physical optics model given by second and third order diffraction theory [36].

### 2.1.3 Design Concepts and Ranking

To develop the Van Atta retroreflector, the following steps were used after the model was built and validated.

1. Develop array concepts and incorporate designed antenna.
2. Simulate RCS with plane wave at various angles of incidence and polarizations.
3. Calculate rotationally-averaged RCS and rank array concepts.

**Table 2.2** Design Evolution and Ranking

Array Concept	RCS Pattern vs Flat Plate	Description/ Evolution	Rot. Avg. RCS* (dB)
		Initial model developed to validate Van Atta operation	2.71
		Theoretical concept by D. Bird. All lines are of equal length.	2.42
		Adaptation of Van Atta Design by Vitaz et. al. Attempts cross-polarized operation using pairs of linear series-fed arrays. Lines differ by $n\lambda_g$ .	3.23
		Removal of one set of lines and patches set to squares.	3.79
		Final Design Reduced inter-array spacing to add more antenna pairs. Overall line length difference is $7\lambda_g$ .	4.77

\*rotationally averaged RCS is normalized to a flat plate of the same size



The design concepts in Table 2.2 are listed in order from worst to best performing. Only those that exceeded the rotationally averaged RCS of a flat plate of the same size were considered viable. Aside from have a significant RCS off-normal, it became a subgoal to also make the retroreflector operate in both polarizations. Using the center transmission line as a guide, “co-polarized” refers to electric fields in line with it along with the x-axis as shown; “cross-polarized” electric field is perpendicular along the y-axis. The normalized RCS for both modes is given in Figure 2.5. It is clear to see that there is a significant improvement in terms of RCS against that of a flat plate, dropping to -10 dB only after  $\theta = 30^\circ$  whereas the flat plate does the same at  $\theta = 5^\circ$ .

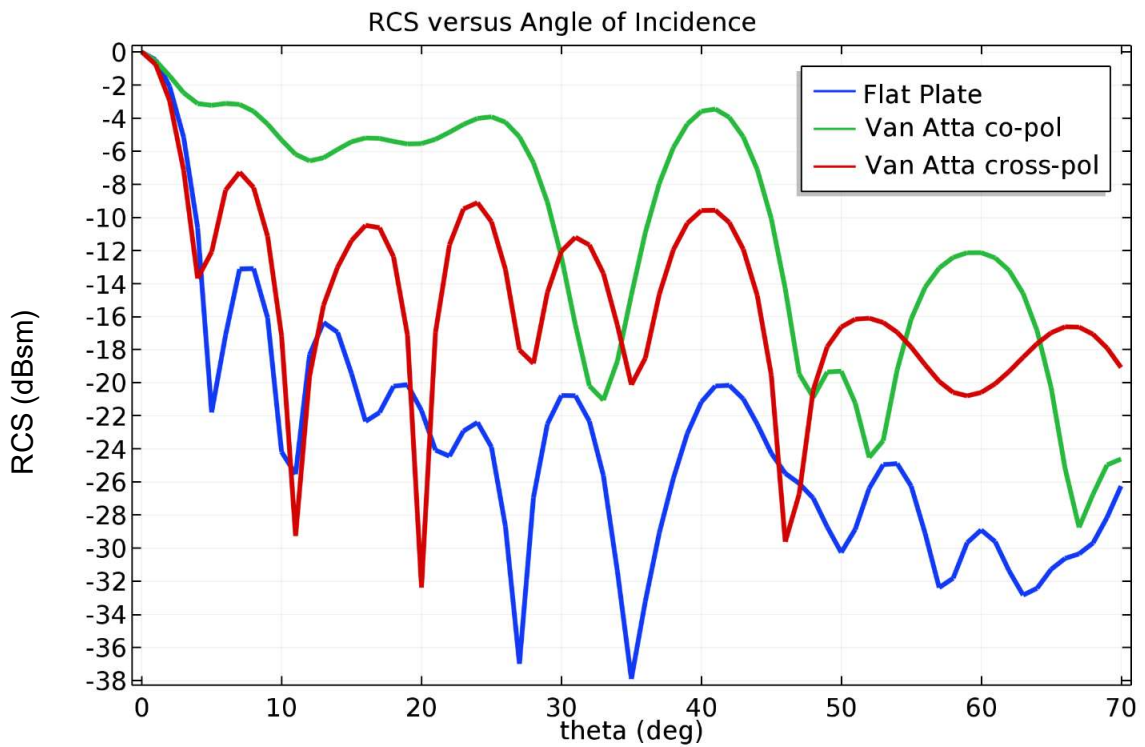


**Figure 2.5** Normalized simulated RCS of final design for both co- and cross-polarized measurements.

## 2.2 Fabrication

Once the final design was chosen, it was fabricated using a precision micro-dispensing tool. This was chosen over inkjet printing due to the ability to produce functional and consistent prints at sub-millimeter scale. Inkjet or drop-on-demand printing, though fully capable of producing samples at this size, can be limiting in terms of usable material that meet certain physical properties, such as viscosity and surface tension. For the Van Atta retroreflector, silver flake paste (Novacentrix Metalon FG77, 85% loading) was dispensed onto a single-sided copper-clad polyimide laminate (DuPont Pyralux LR9220,  $\epsilon_r = 3.6$ ). Prior to printing, the substrate was cleaned with acetone and isopropyl alcohol.

### 2.2.1 Micro-Dispensing (nScript 3Dn and SmartPump)

Patented by nScript Inc., the SmartPump is capable of micro-dispensing materials with high precision. It is a positive pressure pump with a digitally controlled valve that regulates the flow of the material onto the desired surface [37]. The open and closed positions of the valve and applied pressure can be calibrated to the material's properties. The material is loaded into a syringe, centrifuged to remove air pockets, and pumped through a ceramic nozzle tip (50  $\mu\text{m}$  inner diameter, 100  $\mu\text{m}$  outer diameter). The size of the tip generally dictates the limitations on feature size. Smaller tips were available but not needed for the size of the retroreflector's features. Also, a smaller resolution equates to more passes and, subsequently, increased print times and potential for misprints.

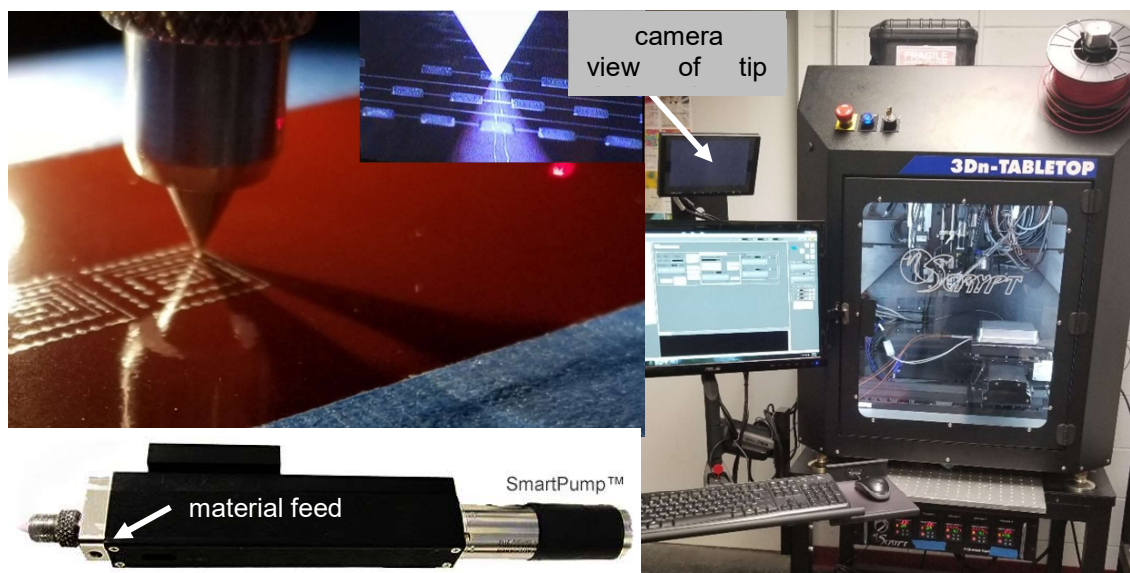


**Figure 2.6** (top) Close-up view during print. The 50  $\mu\text{m}$  tip maintains a print height of 5  $\mu\text{m}$  above the substrate. A camera allows the user to determine quality in situ. The SmartPump (bottom left) uses positive pressure on a syringe to dispense material. The nScript 3Dn-Tabletop (right) is programmed and controlled through proprietary software.

The SmartPump is one of the tools available for use on an nScript 3Dn-Tabletop and its variants. The system used in development of the retroreflector also employed a laser sensor to accurately map the substrate before dispensing. This played a crucial role in the final quality of the sample. The height above the substrate directly correlated with the amount of material pushed through the nozzle, but being too close would prevent any material flow. The ability to follow the small changes in the height of the substrate (which likely varies even every 50  $\mu\text{m}$  across the surface) allowed the print to maintain a fixed gap and produced consistent samples. In addition, a vacuum chuck was used to fix the position of the substrate and improve flatness. Two calibrated system cameras allow views of the prints in situ, which aid in quality control and preliminary analysis.

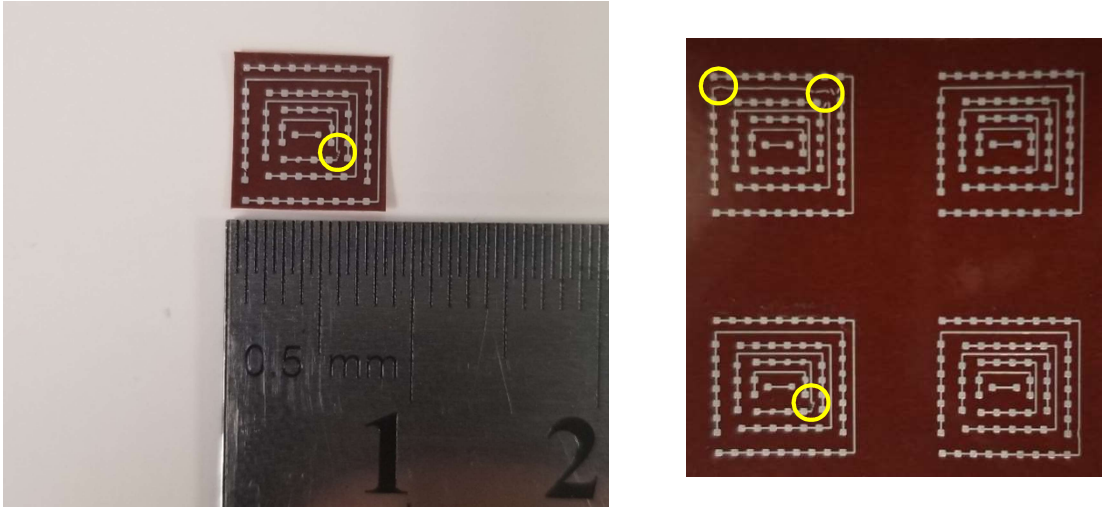


**Figure 2.7** Fabricated samples of individual and array of Van Atta THz retroreflectors. Note the defects circled in yellow. These were likely due to poor adhesion to the substrate prior to sintering.

After printing, the samples were sintered in a vacuum oven at 150° C for 10 minutes. Excess substrate was then trimmed off to complete the sample, shown above in Figure 2.7 before characterization. Care was taken not to warp the sample during this process as small bends could alter the direction of the retroreflected signal during measurements.

### 2.3 Characterization

Once complete, the samples were observed through a calibrated 10x optical microscope for measurements of printed dimensions. This also allowed closer analysis of print quality and consistency. Verification of the printed dimensions ensures operation of the retroreflector as simulated.

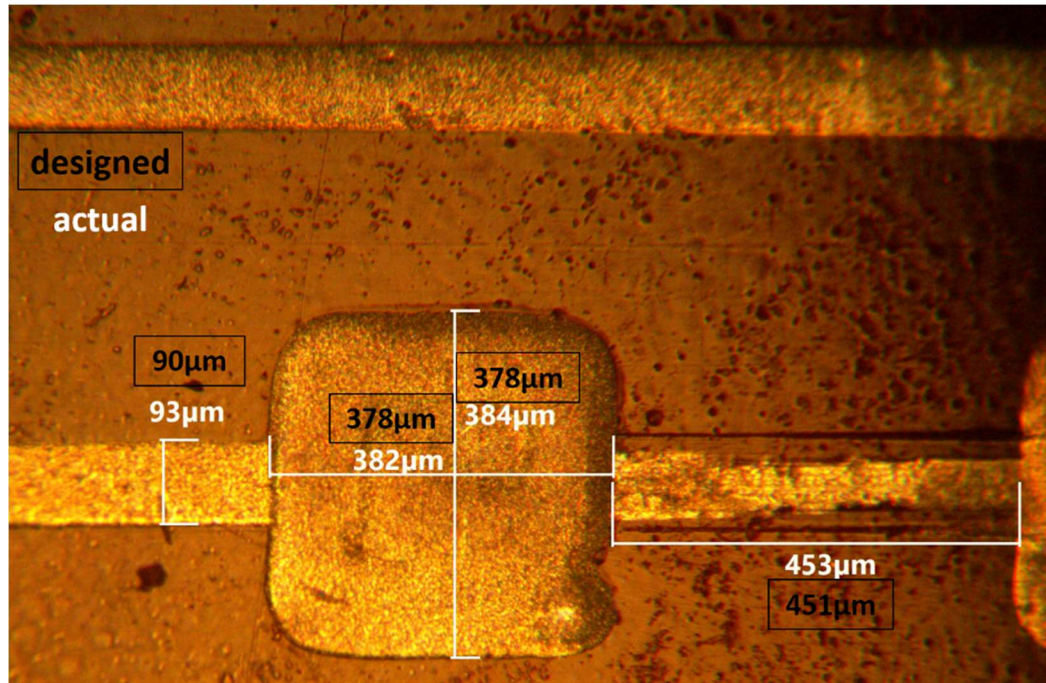


**Figure 2.8** Dimensions of printed sample as measured through 10x digital optical microscope. Note the irregular shape of a square-designed antenna.

All dimensions listed in Table 2.1 were confirmed to be within 7  $\mu\text{m}$  of the design. The most variation was seen in the width of the transmission lines, where such a deviation does not induce as much an effect as does a variation in the length of the patches or intra-antenna lines. Inherent issues of the printing method include rounded corners and blemishes at the print head's lift-off points, such as the bottom right corner of the patch in Figure 2.8.

### 2.3.1 Terahertz Time-Domain Spectroscopy

For this thesis, characterization was completed using a Picometrix (now Luna TeraMetric) T-Ray 2000, a THz time-domain spectroscopy (THz-TDS) system. Using a Ti:Sapphire femtosecond laser as pump-probe, the system generates and detects an electromagnetic transient through the following [38]:

1. Split laser pulse into two beams, pump and probe.
2. Delay the path between the two beams with a mechanically controlled optical delay.
3. Generate the THz pulse by exciting a photoconductive antenna. Carriers are accelerated by a bias voltage
4. Guide the pulse to the sample in transmission or reflection mode
5. Merge the THz pulse and probe at the detector, another photoconductive antenna, which induces a current proportional to the amplitude of the electric field.

The THz pulse is measured over a time window as short as 80 ps. Thus, the output of the system is the amplitude of the electric field over the duration of the optical delay. In order to recover spectroscopic data, a discretized Fourier Transform of the data is required. The T-Ray analytical software recommends time windows for measurements based on powers of 2 in order to accurately perform the Fourier analysis without zero padding. Long scans, up to 2.4 ns, are possible with scan rates up to 50 ps/s. These longer scans, after taking the Fourier transform, correspond to better resolution in the frequency domain.

Issues with this system are inherent to THz-TDS. Because the signal is broadband, power at a given frequency is not fixed. In general, the lower frequencies (0.1-0.4 THz) have more power than the rest up to 3 THz. For measurements of this type, averaging will help regulate fluctuations but come at a cost of slower measurements. This leads to the next problem, as explained in the background information, the atmospheric loss. Changing conditions such as humidity, even within an hour, can have effects on the consistency of the data. A balance between length of the scan window and the overall time between first and last scans is important to maintain.

### 2.3.2 Measurement Schemes

Since the objective is to characterize the ability to retroreflect, the system was set up to take measurements in reflection mode. This setup, shown in Figure 2.9, use a beam splitter to establish a collinear alignment of the transmitter and receiver. The beam, with a spot size of approximately 2.5 cm is directed to the sample on a rotation stage. The sample itself is mounted on a custom, 3D-printed PLA ring with polyethylene foam. Both of these materials are very transparent in the THz band, providing minimal interference with the measurements over traditional metallic mounts. In this orientation, the electric field of the linearly polarized THz beam is orthogonal to the plane of incidence, which is the surface of the bench. The sample can be oriented to take co- and cross-polarized measurements.

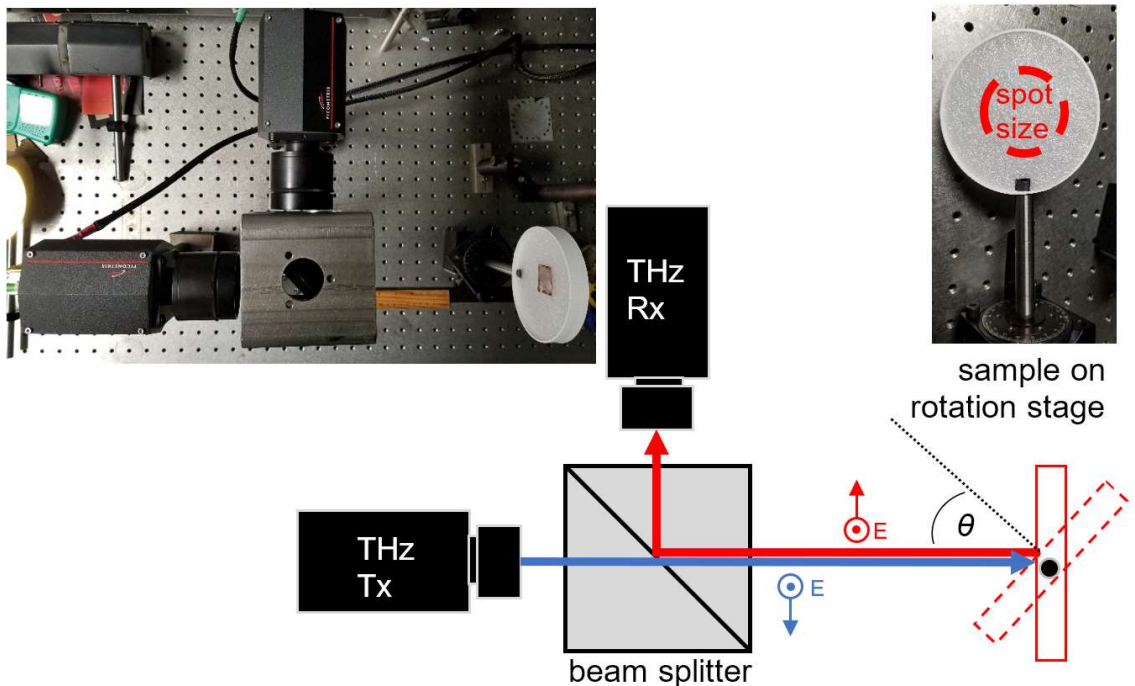


**Figure 2.9** Measurement setup for characterization of Van Atta retroreflector using THz-TDS.

A gold mirror in place of the sample is used to optimize the alignment of the setup. Once this is complete, measurements are taken using the long scan feature with a time window of 512 ps. This corresponds to a frequency resolution of approximately 1.8 GHz, which should be sufficient to determine response of the sample at given frequencies. The scan rate is set to 10 ps/s to strike the balance between speed and accuracy. The following measurements are taken:

1. Gold mirror (3 averages)
2. Blank sample holder (3 averages)
3. Flat metal plate (copper side of blank substrate, same size as sample)
  - a. 0 - 20° every 1°
  - b. 25 - 70° every 5°
4. Individual sample of Van Atta retroreflector
  - a. 0 - 20° every 1°
  - b. 25 - 70° every 5°
5. 2 x 2 array of Van Atta retroreflectors
  - a. 0 - 20° every 1°
  - b. 25 - 70° every 5°

Once the measurements were complete, the time-domain data was exported to MATLAB for Fourier analysis and postprocessing using the Fast Fourier Transform function. The code is supplied in Appendix B.



## CHAPTER 3

### RESULTS AND DISCUSSION

#### 3.1 Performance Data

All simulation data from COMSOL and time-domain measurement data from T-Ray 2000 was imported into MATLAB for analysis and presentation. The same format for comparing simulation to measurement was taken for the flat plate and the Van Atta retroreflector in co-polarized and cross-polarized orientations. The flat plate once again serves as the test of the methods used.

First, the frequency response is examined by looking at the peak RCS values and comparing the location to that predicted in the simulation. Next, the electric field intensity as a function of angle of incidence and frequency is presented. The presence of high values, or “hotspots”, along a frequency band indicates Van Atta behavior. Finally, the total power and power by frequency versus angle of incidence is compared to the flat plate and Van Atta simulation results.

##### 3.1.1 Flat Plate Measurements

As shown in Figure 3.1, RCS values at two different polar angles do not show any resonant response near the design frequency of 200 GHz. This is expected since the frequency response of a flat plate should not present any distinct peaks off-normal. In Figure 3.2, the measured electric field intensity as a function of frequency and polar angle is shown for the flat plate. Note that the large values all occur near normal incidence (0 degrees) and are roughly independent of frequency as would be expected for a flat plate. The key points are the RCS value has a

sharp peak near normal and there is no obvious resonance near 200 GHz. For intensity along a frequency band, one should expect low values as the polar angle increases, with no distinct “hotspots”.

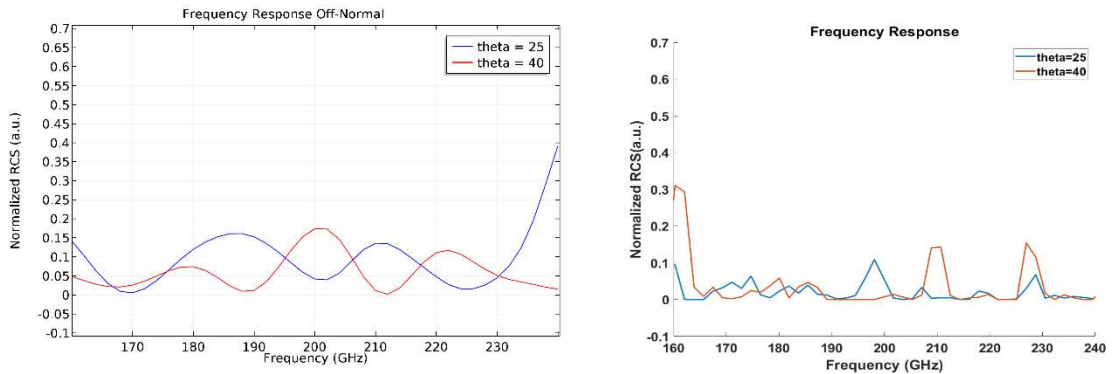


**Figure 3.1** Simulated (left) and measured (right) RCS frequency response of flat plate at polar angles of 25° (blue) and 40° (red). No significant peaks are found, as expected.

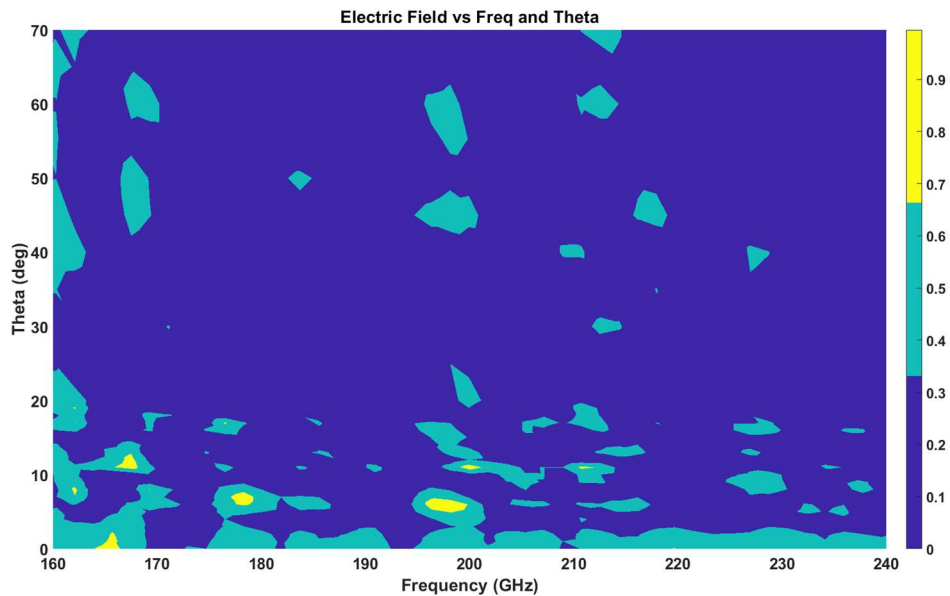


**Figure 3.2** Hotspot plot of flat plate. Higher values are found toward normal incidence with no clear peak values off-normal.

A comparison is shown in Figure 3.3 for the total normalized power (i.e. integrated over all frequencies) versus the simulation results for the flat plate and the Van Atta. Note that the measured total power versus angle follows the trend for the simulated flat plate up to approximately 5°. Since the simulated flat plate results are for a specific frequency, the sidelobe peaks near 7, 13, 18 degrees which are due to diffraction/ interference are clearly visible. However, since the experimental data is averaged over all frequencies, the sidelobe structure is averaged out. This will show to be an inherent limitation with the characterization tool.

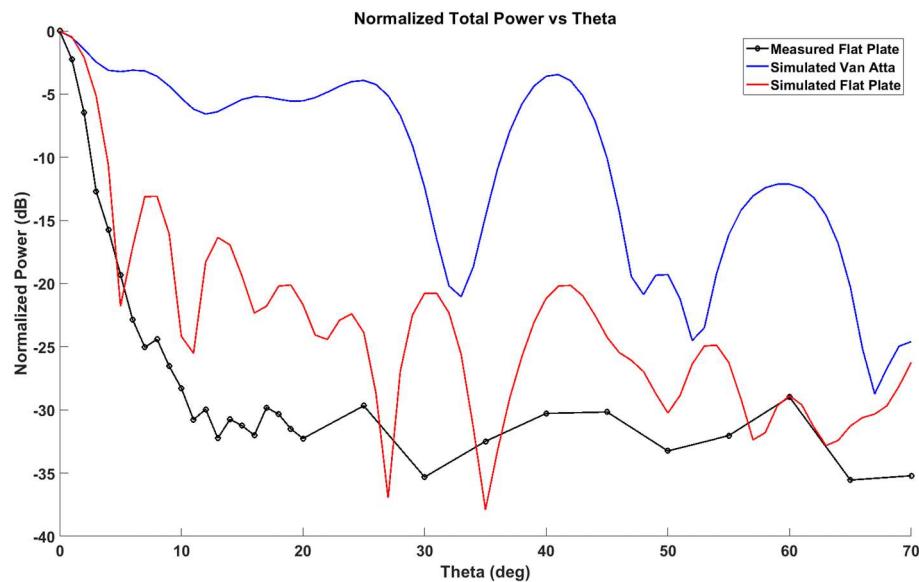


**Figure 3.3** Total power as a function of angle for a flat plate. The characteristic sharp drop from 0-5° is indicative of flat plate response, but subsequent lobes are not. This stems from averaging over all frequencies in the measured values instead of a single frequency, as done in the simulation.

In comparing the measured results from a Van Atta structure to the theoretical predictions, we focus on two key features which would indicate Van

Atta behavior: (a) a resonant response close to the design frequency of 200GHz and (b) compared to a flat plate, enhanced RCS values at large angles of incidence (i.e. greater than 10°).

To analyze the experimental response for resonant behavior in the presence of experimental noise, the RCS versus incident angle is plotted for frequencies both close to resonance and far from resonance. As shown in Figure 3.4, when the experimental data for the flat plate is analyzed, there does not appear to be much difference between the resonant and non-resonant RCS values. In order to remove the noise, the data from several of the resonant frequencies as well as non-resonant frequencies are averaged as shown in Figure 3.5. Note that the experimental data is a better match for the flat plate rather than for the Van Atta simulation results.

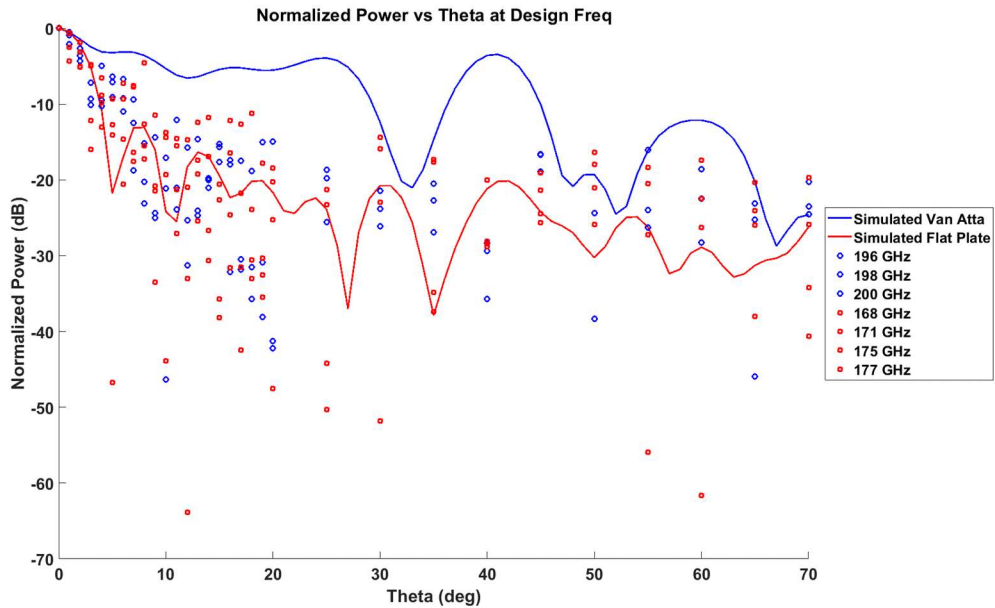


**Figure 3.4** Normalized power by frequencies for a flat plate that correspond to resonant (blue markers) and non-resonant bands (red markers). These are presented as a comparison for the Van Atta retroreflector below.

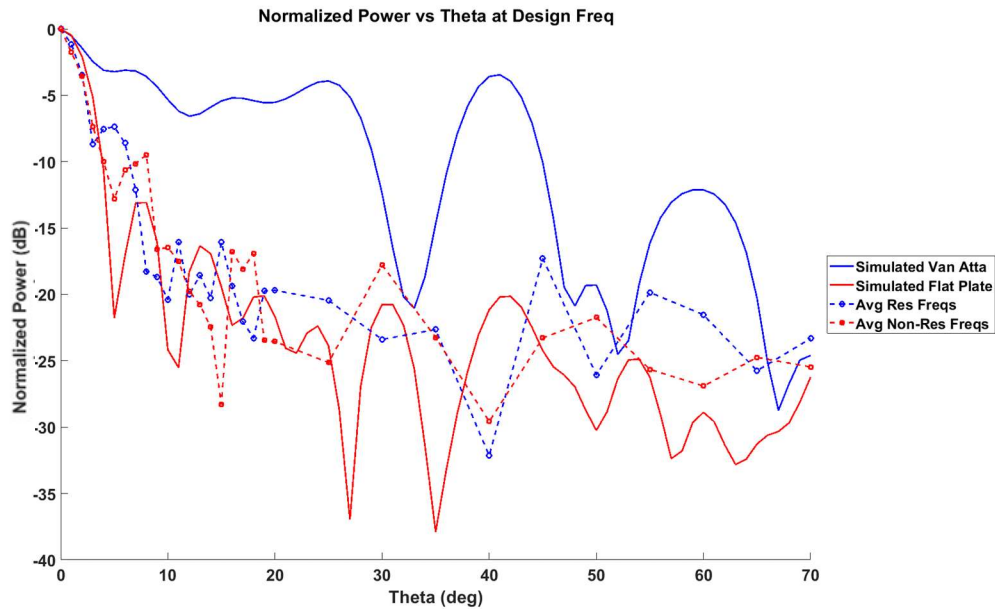


**Figure 3.5** Averaged values of the previous figure to show the trend for the flat plate measurement. Note both bands adhere to the flat plate simulation.

### 3.1.2 Co-Polarized Van Atta Measurements

In the previous section, it was shown that experimental results from the flat plate RCS measurements are consistent with simulation results for a flat plate: (a) there is no resonant behavior observed near 200 GHz and (b) the angular dependence of the RCS closely follows the simulation results. In this section, we perform the same data analysis for experimental data from the Van Atta structures in the co-polarized mode.

As shown in Figure 3.6, there is clearly a resonant response near the design frequency. Once again, both curves are presented at polar angles 25° and 40° (these values chosen as expected high value points for the RCS). The measured response did not exhibit as strong a response for 25° but did present a local peak

value. It is worth noting that the actual frequency response was detected at 199 GHz rather than the simulated 196 GHz.

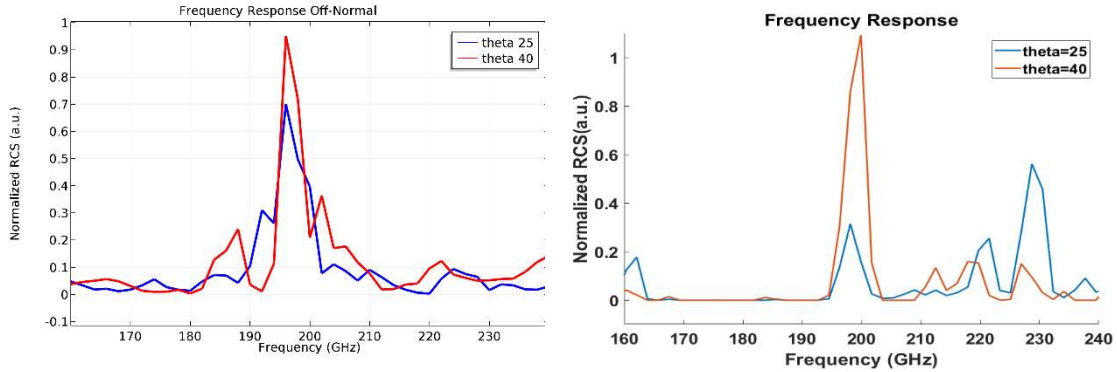


**Figure 3.6** Simulated (left) and measured (right) RCS frequency response of co-polarized Van Atta retroreflector taken at  $\theta = 25^\circ$  and  $40^\circ$ . The simulation predicted a response at 196 GHz, while measurements centered about 199 GHz. This 1.5% shift is discussed later.

In Figure 3.7, the experimental electric field intensity for the Van Atta retroreflector as a function of angle and frequency is shown. Note the “hotspots” at large angles near the design frequency of 196 GHz. This is an indicator that the retroreflector is operating as expected, providing improved performance off-normal over the flat plate seen in Figure 3.2.

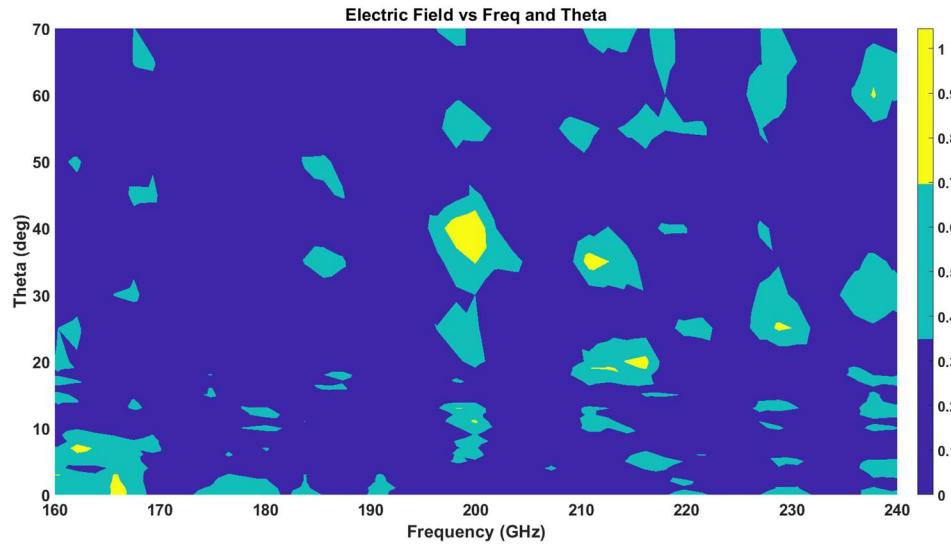


**Figure 3.7** Hotspot plot for co-polarized Van Atta shows a strong off-normal peak with a band of mid-range values in line around the design frequency. This is a good indication of proper Van Atta operation.

In order to be consistent with the analysis for a flat plate presented in the previous section, Figure 3.8 shows the total normalized power for the Van Atta retroreflector. Note that the response, which again is averaged over all frequencies, follows the general trend for a flat plate. This is not surprising since one would expect the Van Atta retroreflector to behave like a flat metal plate except when the electromagnetic frequency is in resonance. Since only a small fraction of the total THz spectral power from the time-domain measurement is in resonance with the structure, one would expect the non-resonant response to dominate in this case.

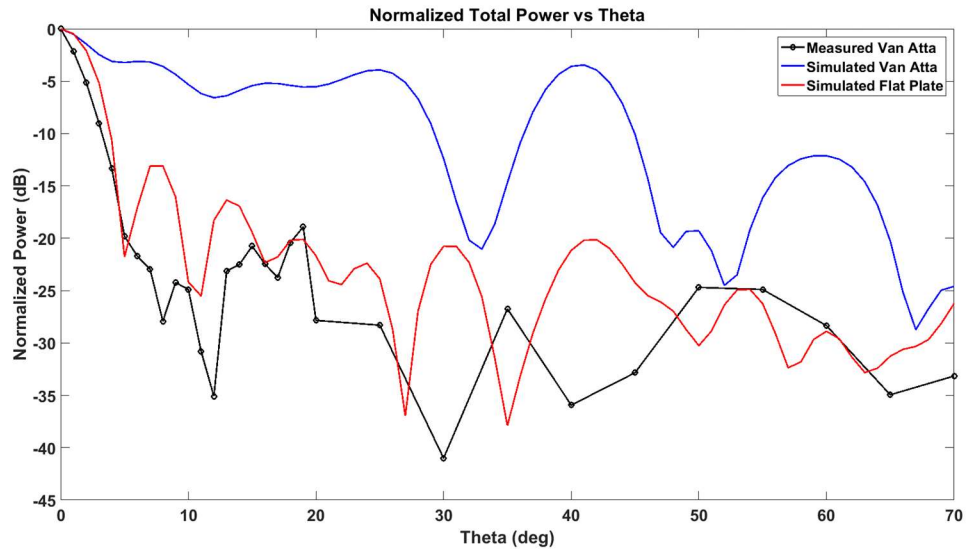


**Figure 3.8** Normalized total power for the co-polarized Van Atta retroreflector. Since this represents many frequencies, one should not expect the Van Atta response but rather one similar to a flat plate, as seen.

In order to sufficiently compare the resonant versus non-resonant response of the Van Atta array, the measured response at several frequencies close to the resonant frequency and away from the resonant frequency are shown in Figure 3.9. Clearly from this data, the close to resonant frequency response is clearly larger than the off resonant response.

In order to better visualize the data, one must again reduce the noise in the THz reflectivity data. To accomplish this, the RCS frequency response of the resonant frequencies are averaged together as shown in Figure 3.10. Likewise, the RCS frequency response from several non-resonant frequencies are averaged together. Clearly, the resonant frequencies are consistent with the simulated Van Atta response while the non-resonant frequencies are consistent with a flat plate response.



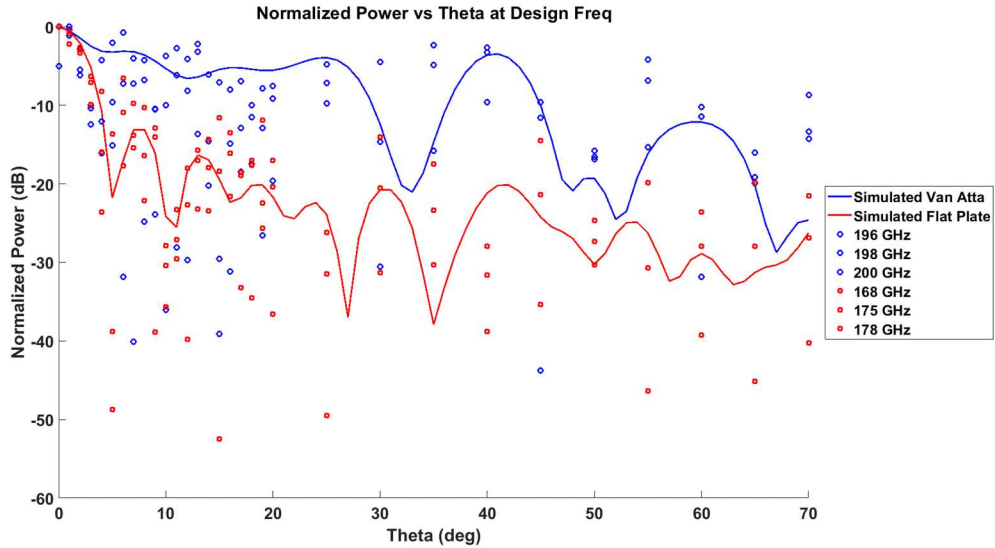


**Figure 3.9** Normalized power by frequency for the co-polarized Van Atta retroreflector. The specific frequencies were chosen based on the simulation as resonant (blue markers) or non-resonant (red markers). Note the prevalence of resonant frequency points in higher power regions.

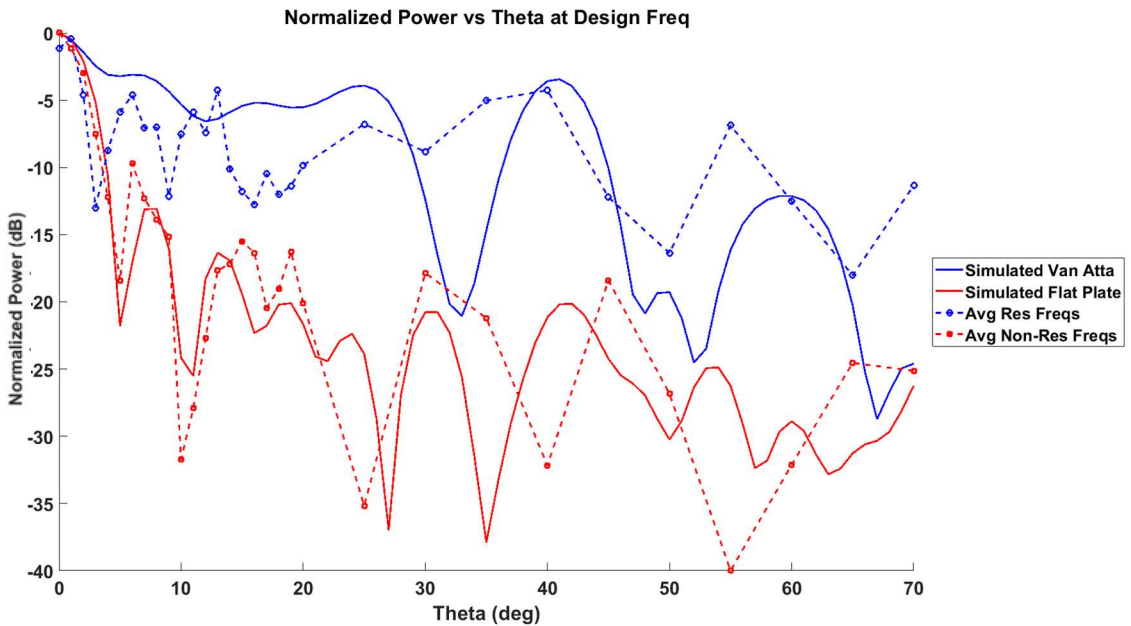


**Figure 3.10** Averaged values for resonant and non-resonant bands for the co-polarized Van Atta retroreflector. The blue dashed line follows the general path of the Van Atta simulation, averaging above -10dB out to a considerable angle. This is the most clear indication of Van Atta operation, as the non-resonant bands behave as flat plates.

In summary, for the co-polarized Van Atta measurements, analysis of the experimental data shows two important features which strongly suggest that the Van Atta design is functioning as a Van Atta retroreflector: (a) there is a resonant response close to the designed resonant frequency and (b) there is an enhanced RCS value for large angles of incidence compared to a flat metal plate.

### 3.1.3 Cross-Polarized Van Atta Measurements

The same analysis done in the previous two sections is conducted for the cross-polarized mode of the Van Atta retroreflector. Figure 3.11 shows the simulated and measured RCS frequency responses. Though a clear response is expected around 188 GHz, no such response is witnessed during the characterization.

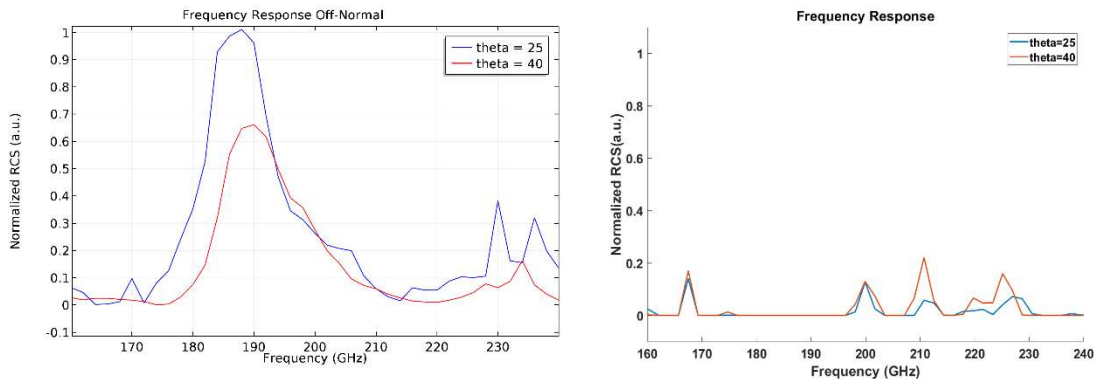


**Figure 3.11** Simulated (left) and measured (right) RCS frequency response of cross-polarized Van Atta retroreflector. Simulation predicted 12 GHz shift from the design, but measurements showed no significant response.

The hotspot plot in Figure 3.12, similar to the one for the co-polarized mode, should show again a clear band of high value at the resonant frequency, but this is not the case. There is no clear response along the predicted resonant frequency band, indicating a lack of Van Atta behavior.

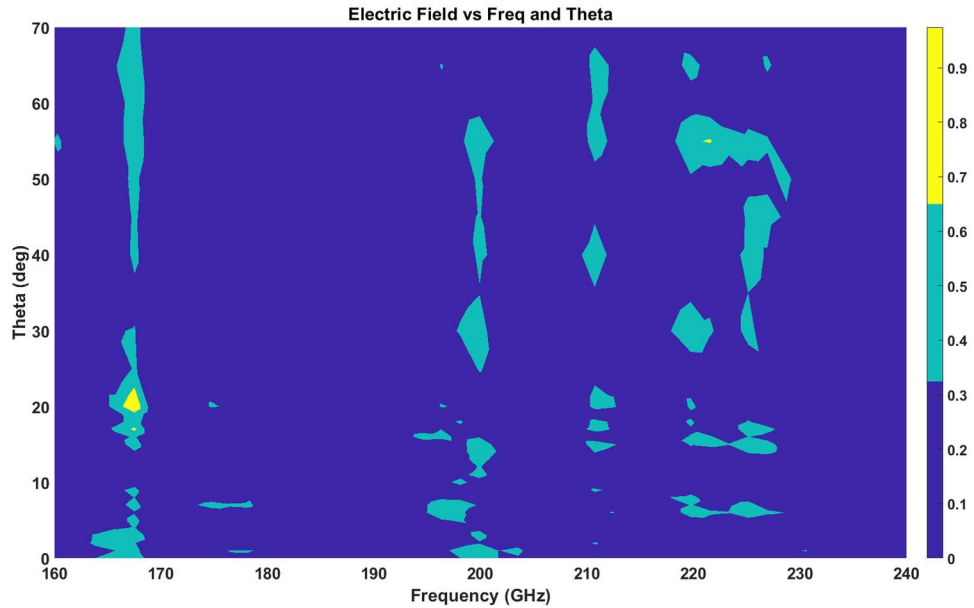


**Figure 3.12** Hotspot plot for cross-polarized Van Atta. There is no clear resonance band as present in the co-polarized mode.

Again, a comparison against a flat plate is shown in Figure 3.13. The response here is similar to the others before – the Van Atta array performs as a flat plate when looking at the average over all the frequencies in a broad THz measurement. This is in contrast to the simulated cross-polarized Van Atta response, also shown.

To further investigate the performance, we again look at the RCS response of frequencies around resonance as well as some bands that are expected to be non-resonant. These values are shown in Figure 3.14. Unlike the same plot for the co-polarized mode, we do not see as prominent a Van Atta behavior.

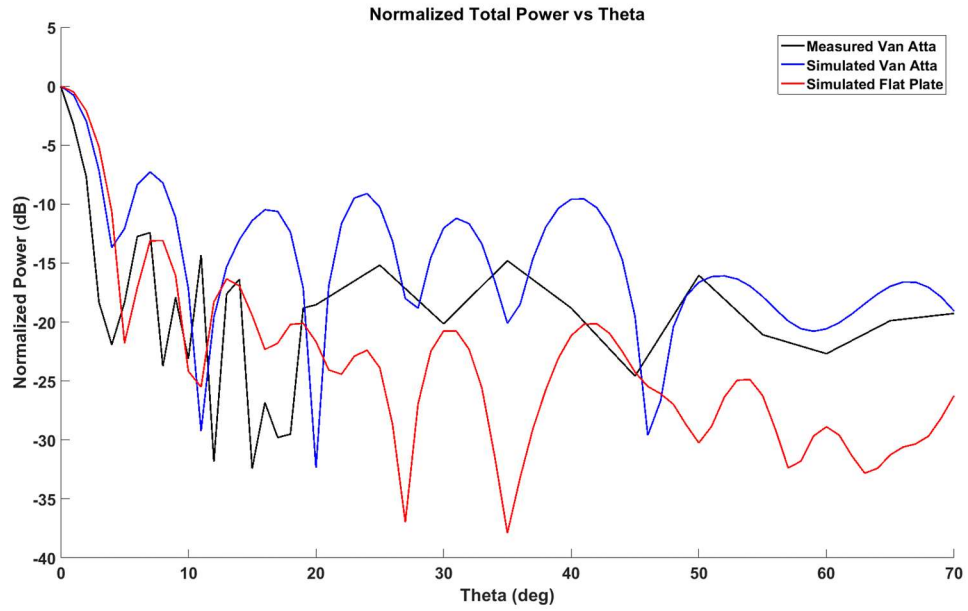


**Figure 3.13** Normalized total power for the cross-polarized Van Atta retroreflector shows the flat plate pattern as expected.

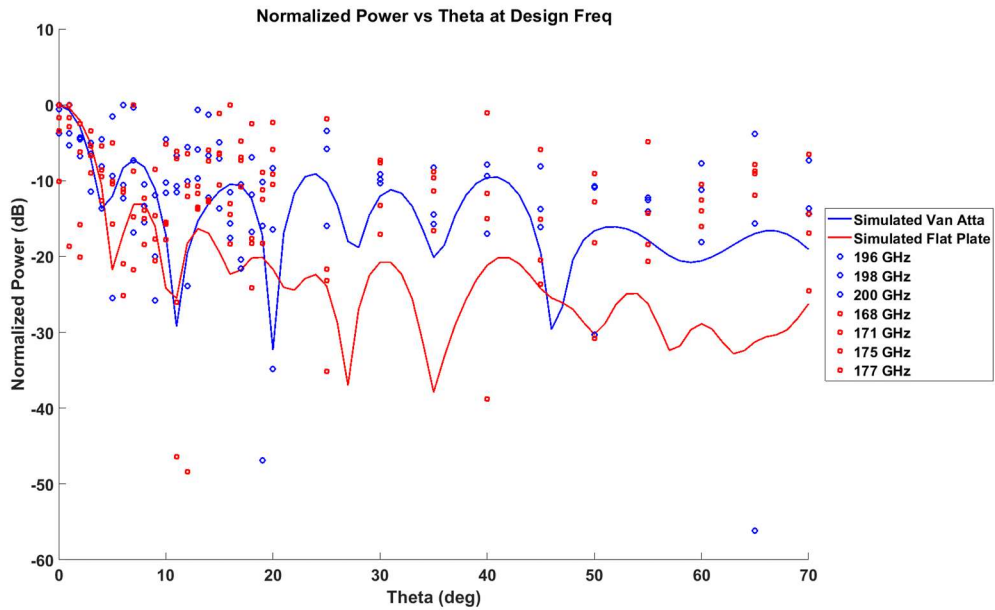


**Figure 3.14** Normalized power by frequency for the cross-polarized Van Atta retroreflector. This shows no clear difference between resonant and non-resonant bands.

Looking at the averages of those RCS values at resonant and non-resonant bands in Figure 3.15, it is shown there is a slight indication of Van Atta behavior, averaging an RCS response approximately 5 dB higher than the flat plate. But the lack of adherence to the simulated shape of the curve as well as the variation of the non-resonant response with respect to the flat plate leads to the conclusion that this structure did not fully operate as intended and/or the measurement was unable to detect its performance.

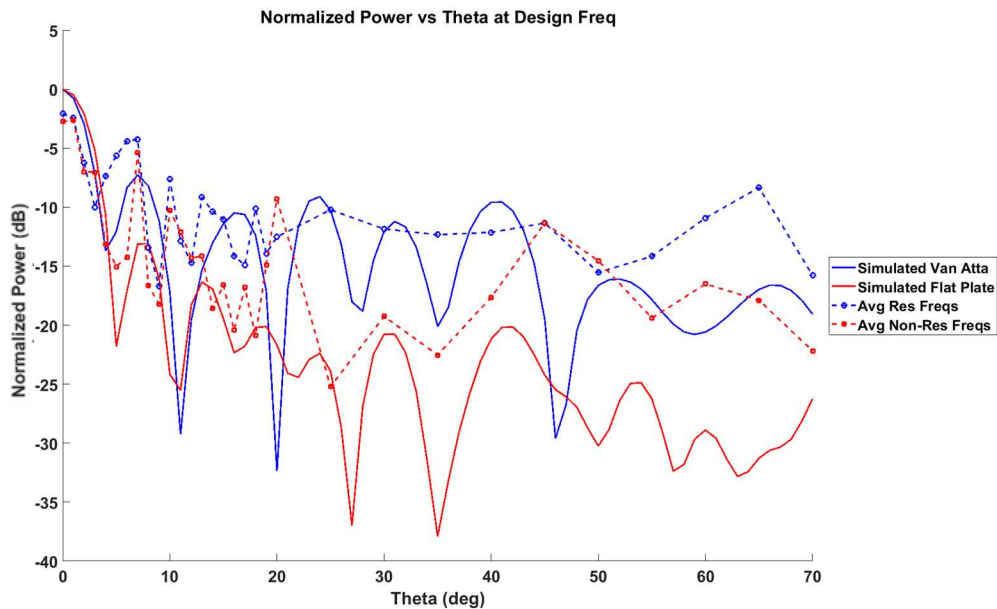


**Figure 3.15** Averaged values from previous figure for the cross-polarized Van Atta retroreflector. The resonant frequencies averaged 5 dB higher overall but generally followed the shape of the flat plate response.

### 3.2 Discussion

As seen from the co-polarization data presented, the fabricated Van Atta retroreflector does indeed improve RCS over wider angles of incidence. It does not, however, perform as close to the simulation as hoped.

One likely issue is systemic in this study, the use of THz-TDS. As a pulsed system, it relies on the optical delay to accurately recreate the waveform. The Van Atta array design has transmission lines of varying lengths, and even though they are of equal electrical length, it presents a problem for the time-domain measurement of short THz pulses. The delays in the Van Atta designs are ideally all equal. However, for the design described in Chapter 2, the delays are integer multiples of a wavelength which enables more complicated patterns to be created in a smaller area. For this chosen design, the delays among the different transmitter-receiver pairs vary between 1 and 8 wavelengths. Since the delay caused by one wavelength is approximately 3 ps, which is comparable to the duration of the electromagnetic transient, a corresponding variety of delays between 3 and 24 ps means that even if an initially planar THz wavefront from the THz pulse is reflected from the structure, the time delay results in a non-planar reflected wavefront. Clearly, if the incoming radiation were continuous and not a short pulse, the integral wavelength delays would not be an issue. However, as the THz pulse duration becomes comparable to the delays in the Van Atta design, one can expect a degradation in the Van Atta response.

Another problem is the variation of power at any given frequency. The need to have consistent measurements of power, especially for the resonant frequencies, is crucial in determining if the device operates correctly. Clearly, using a broadband THz pulse to resolve a relatively spectrally narrow response is not the optimal experimental method to characterize the Van Atta structure. While resolution of the specific frequency could be achieved by increasing the time-

domain scan window, there is a limit to this methodology due to the inherent noise in the THz time-domain system. Moreover, this in turn increases the time required to perform a full measurement over the angles of incidence. Longer times between the first and last scan can introduce error brought on by changing lab conditions. In order to improve the quality of the measurement data, a tunable continuous-wave THz system would be preferable to a THz time-domain measurement system.

The printing method is shown to produce working samples, but there is room for improvement. Variations and defects in the print are also very likely to cause the samples to deviate from their simulated performance. In some areas, the silver paste was too thin or flaked away from poor adhesion. Also, misprinted antennas and lines can induce losses and inefficiency with irregular or incomplete shapes.

The cross-polarized mode was very disappointing. Though not a major design objective, the ability to use the same structure for two modes of operation is appealing. Simulations suggested an improvement over the flat plate, though not as great as the co-polarized mode. The experiment seems to confirm the cross-polarized mode's response as akin to the flat plate's with slightly more power. A possibility for this low response could be greater losses to grating lobes than expected. Array spacing should be kept less than a half-wavelength to avoid any grating lobes. Due to the arrangement chosen and line lengths required, exceeding this spacing was unavoidable. Exploring different ways to construct the array is necessary to address this issue.

Finally, the frequency response for the co-polarized mode was shifted by 3 GHz. Though only a 1.5% change, it almost represents half of the spectral width. Some of it can be explained by the resolution of the scan after the Fast Fourier Transform (approximately 1.8 GHz), but the likely issue stems from inaccurate material properties for the substrate. The manufacturer's data did not extend into the THz band; the dielectric constant thus had to be extrapolated. Also, defects in the print once again can affect performance. The printed dimensions were approximately 1.5% larger than designed. This, however, would have shifted the frequency lower instead of higher.



## **CHAPTER 4**

### **CONCLUSION**

#### **4.1 Conclusions and Future Work**

Van Atta arrays can be a solution to implement smart steerable antenna systems for THz wireless communication. They can be easily manufactured and incorporated into necessary subsystems. More research and experimentation is required to determine the capabilities and limitations of Van Atta arrays in this context, especially integration of active components. Following the trends in other bands, the THz gap may soon see the light. This thesis focused on the design, fabrication, and characterization of an initial prototype for a passive planar THz retroreflector.

The design emphasized a Van Atta retroreflector which exhibited high reflectivity for both polarizations over a broad range of angles of incidence. Simulations showed a significant response near the design frequency, with approximately 10-15 dB improvement over a flat plate. The fabrication tool used for this design was an nScrypt Tabletop 3Dn. The ability to precisely microdispense conductive material with consistency and accuracy was critical to the success of the prints. The samples were characterized with THz time-domain spectroscopy to determine their performance as Van Atta arrays. The co-polarized mode showed significant Van Atta behavior, resembling that of its simulated average 10 dB improvement over a flat plate of comparable size.

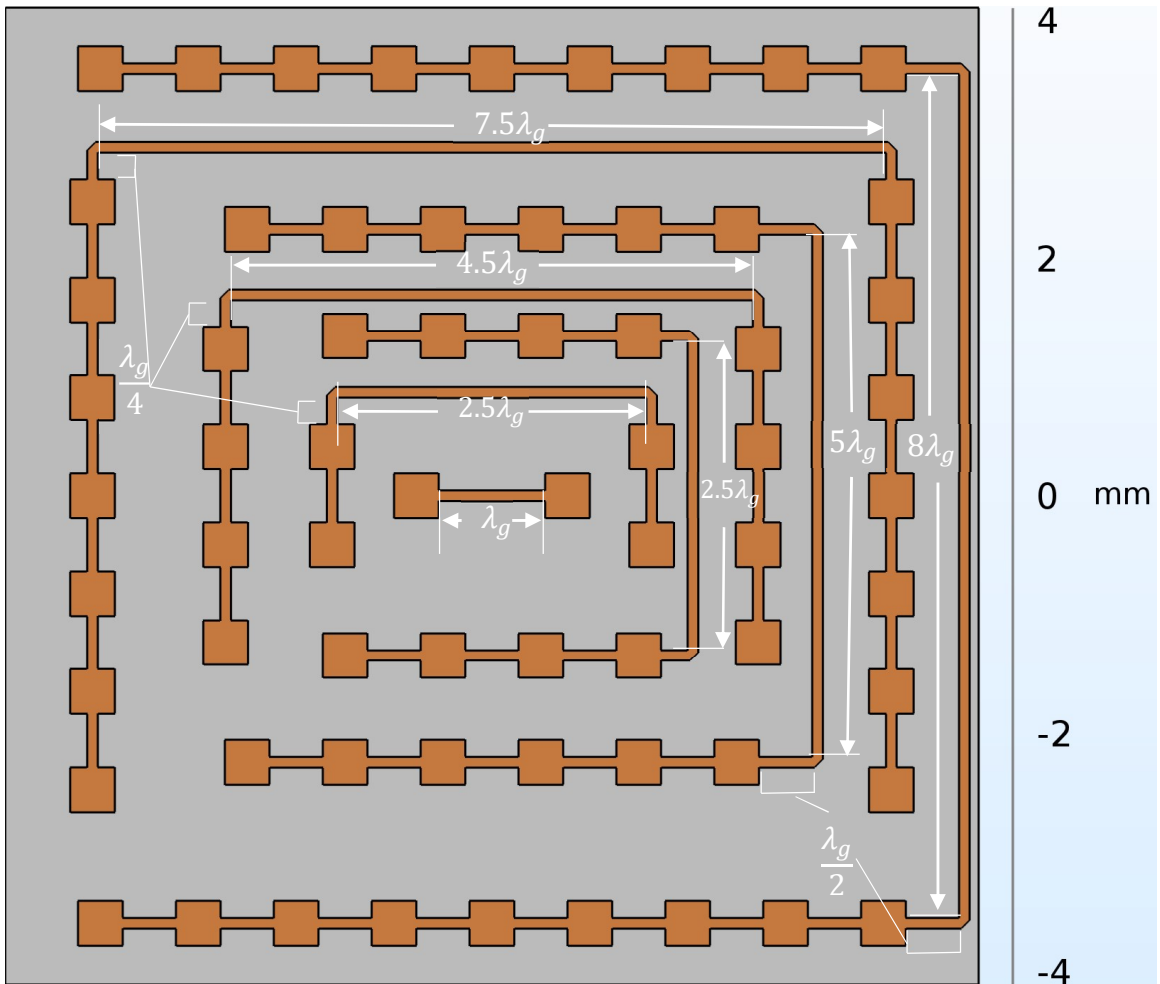
The cross-polarized mode, however, did not present clear evidence of such behavior, though a response was detected.

Future work in this can seek improvement in all three aspects of the objective. Further optimization of the design can focus on the tradeoff between size and gain. Decreasing the lengths of the lines and using smaller sub-arrays may also help reduce the grating lobes. More precise fabrication techniques such as a methodical print sequence and layering may help improve quality and robustness of the samples. New measurement techniques or equipment such as continuous-wave systems can be used to better characterize the samples. All of these can help determine the viability of Van Atta retroreflectors as critical components for THz wireless communications.

## APPENDIX A

### DESIGN DIMENSIONS

Schematic showing the dimensions of the final design for the Van Atta retroreflector.



$$\lambda_g = 851.6\ \mu\text{m}$$

Each square patch is  $L = W = 377.9\ \mu\text{m}$

Patches within any linear series are connected by lines of length  $\lambda_g/2$

All transmission lines are  $90\ \mu\text{m}$  wide.

Line lengths shown (e.g.  $8\lambda_g$ ) are measured along inner edge.

## APPENDIX B

### MATLAB CODES

#### B.1 MATLAB code to iterate antenna calculations.

%% This code incorporates the calculations necessary for antenna design based on frequency and substrate properties

%% set constants

```
c = 2.998e8;  
f = 200e9;  
sub_eps = 3.6;  
H = 52e-6;  
Wline = 90e-6
```

%% starting points

```
eps_eff = sub_eps;  
W = c/(2*f*sqrt((eps_eff+1)/2))
```

%% iterate for square patches

```
i=0;  
while i<10  
    eps_eff = ((sub_eps+1)/2)+((sub_eps-1)/2)*(1/sqrt(1+(12*H/W)));  
    i=i+1;  
    Leff = c/(2*f*sqrt(eps_eff));  
    dL = 0.412*H*(((eps_eff+0.3)*((W/H)+0.264))/((eps_eff-0.258)*((W/H)+0.8)));  
    L = Leff-2*dL  
    W=L  
    %W=Wline;  
end
```

%% estimate impedance

```
Zline = (376.73/sqrt(eps_eff))*(W/H+1.393+0.677*log(W/H+1.444))^-1;  
Zant = 1/(2*(W*(1-(2*pi*H/lambda)^2/24)/(120*lambda)));
```

**B.2** MATLAB code to call import function and perform fast Fourier transform on time-domain data for spectral analysis.

```
clear all
```

```
%%set frequency range and file structure
```

```
freqstart = 100;
```

```
freqend = 500;
```

```
directory = "FILE_PATH_HERE";
```

```
filename = "vanatta";
```

```
%% import files with time-domain data using importTRay.m and create array of FFT values
```

```
theta=[0:1:20 25:5:70];
```

```
for i=1:numel(theta)
```

```
    if theta(i)<10
```

```
        s1 = directory+filename+"_0"+int2str(theta(i))+".txt";
```

```
    else
```

```
        s1 = directory+filename+"_ "+int2str(theta(i))+".txt";
```

```
    end
```

```
    [t(:,i),v_t(:,i)] = importTRay(s1);
```

```
    dnu = 1/(t(end,i)-t(1,i));
```

```
    nu = (0:(3/dnu))*dnu;
```

```
    v_nu1(:,i) = abs(fft(v_t(:,i)));
```

```
    if i<2
```

```
        v_nu = [v_nu1(1:length(nu))];
```

```
    else
```

```
        v_nu = [v_nu v_nu1(1:length(nu),i)];
```

```
    end
```

```
end
```

```
%% repeat for background FFT
```

```
[bt,bv_t] = importTRay(directory+'blanklongscan.txt');
```

```
bdnu = 1/(bt(end)-bt(1));
```

```
bnu = (0:(3/bdnu))*bdnu;
```

```
bv_nu = abs(fft(bv_t));
```

```
bv_nu = bv_nu(1:length(bnu));
```

```
%% frequency value mapping to element location
```

```
nustart = find(abs(nu.*1000-freqstart) < 0.9);
```

```
nuend = find(abs(nu.*1000-freqend) < 0.9);
```

```
%% import simulation values
```

```
[theta_sim,v_sim] = importTRay(directory+'vanattasim.txt');
```

```
[theta_sim,fp_sim] = importTRay(directory+'flatplatesim.txt');
```

**B.3** MATLAB function file to import time-domain data from a .txt output file into vectors.

```
function [time,v_t] = importTRay(filename, startRow, endRow)
%% This is a function file used to import time-domain data into a MATLAB
vectors.

%% Initialize variables.
delimiter = '\t';
if nargin<=2
    startRow = 3;
    endRow = inf;
end

%% Format string for each line of text:
% column1: double (%f)
% column2: double (%f)
% For more information, see the TEXTSCAN documentation.
formatSpec = '%f%f%s%s*s%s*s*s*s%[\n\r]';

%% Open the text file.
fileID = fopen(filename,'r');

%% Read columns of data according to format string.
% This call is based on the structure of the file used to generate this
% code. If an error occurs for a different file, try regenerating the code
% from the Import Tool.
dataArray = textscan(fileID, formatSpec, endRow(1)-startRow(1)+1, 'Delimiter',
delimiter, 'EmptyValue', NaN, 'HeaderLines', startRow(1)-1, 'ReturnOnError',
false);
for block=2:length(startRow)
    frewind(fileID);
    dataArrayBlock = textscan(fileID, formatSpec, endRow(block)-
startRow(block)+1, 'Delimiter', delimiter, 'EmptyValue', NaN, 'HeaderLines',
startRow(block)-1, 'ReturnOnError', false);
    for col=1:length(dataArray)
        dataArray{col} = [dataArray{col};dataArrayBlock{col}];
    end
end

%% Close the text file.
fclose(fileID);

%% Allocate imported array to column variable names
time = dataArray{:, 1};v_t = dataArray{:, 2};
```

## REFERENCES

- [1] K. R. Jha and G. Singh, "Terahertz planar antennas for future wireless communication: A technical review," *Infrared Physics & Technology*, vol. 60, p. 71, 2013.
- [2] J. Ma, "Terahertz Wireless Communication Through Atmospheric Turbulence and Rain," PhD Dissertation, Department of Physics, New Jersey Institute of Technology, Newark, NJ, 2016.
- [3] Fujitsu, "Relationship between electromagnetic wavelengths and frequencies," 20110912-01a1\_tcm100-930360.jpg, Ed., ed. Kawasaki, Japan, 2011.
- [4] I. F. Akyildiz, J. M. Jornet, and C. Han, "Terahertz band: Next frontier for wireless communications," *Physical Communication*, vol. 12, 2014.
- [5] A. Redo-Sanchez and X.-C. Zhang, "Terahertz Science and Technology Trends," *IEEE Journal of Selected Topics in Quantum Electronics*, vol. 14, no. 2, pp. 260-269, March 2008.
- [6] J. Federici and L. Moellar, "Review of terahertz and subterahertz wireless communications," *Journal of Applied Physics*, vol. 107, no. 111101, 2010.
- [7] S. Cherry. (2004, July 1) Edholm's Law of Bandwidth. *IEEE Spectrum* [Online]. Available: <http://spectrum.ieee.org/telecom/wireless/edholms-law-of-bandwidth>
- [8] Cisco, "The Zettabyte Era — Trends and Analysis – Cisco," June 7 2017, Available: <http://www.cisco.com/c/en/us/solutions/collateral/service-provider/visual-networking-index-vni/vni-hyperconnectivity-wp.html>, Accessed on: June 19, 2018.
- [9] T. Kleine-Ostmann and T. Nagatsuma, "A Review on Terahertz Communications Research," *Journal of Infrared Millimeter and Terahertz Waves*, vol. 32, pp. 142-171, 2011.
- [10] T. Kurner and S. Priebe, "Towards THz Communications - Status in Research, Standardization and Regulation," *Journal of Infrared Millimeter and Terahertz Waves*, vol. 35, pp. 53-62, 2014.
- [11] J. Federici, J. Ma, and L. Moellar, "Review of Weather Impact on Outdoor Terahertz Wireless Communication Links," *Nano Communication Networks*, vol. 10, pp. 13-26, 2016.

- [12] R. Piesiewicz *et al.* (2007, December) Short-Range Ultra-Broadband Terahertz Communications: Concepts and Perspectives. *IEEE Antennas and Propagation Magazine*. 24-39.
- [13] K. Liu *et al.*, "100 Gbit/s THz Photonic Wireless Transmission in the 350-GHz Band with Extended Reach," *IEEE Photonics Technology Letters*, Article vol. 30, no. 11, pp. 1064-1067, 2018.
- [14] Q. Wu *et al.*, "A 21 km 5 Gbps real time wireless communication system at 0.14 THz," in *International Conference on Infrared, Millimeter, and Terahertz Waves, IRMMW-THz*, 2017.
- [15] J. Shaw, "Radiometry and the Friis transmission equation," *American Journal of Physics*, vol. 81, no. 1, pp. 33-37, 2013.
- [16] M. T. Barros, R. Mullins, and S. Balasubramaniam, "Integrated Terahertz Communication With Reflectors for 5G Small-Cell Networks," *IEEE Transactions on Vehicular Technology*, vol. 66, no. 7, pp. 5647-5657, 2017.
- [17] J. Federici, L. Moeller, and K. Su, "Terahertz Communication," in *Handbook of terahertz technology for imaging and sensing*, D. Saeedkia, Ed. Cambridge: Woodhead Publishing, 2013.
- [18] D. Turchinovich, A. Kammoun, P. Knobloch, T. Dobbertin, and M. Koch, "Flexible all-plastic mirrors for the THz range," *Applied Physics A*, vol. 74, no. 2, pp. 291-293, 2002.
- [19] N. Krumbholz *et al.*, "Omnidirectional terahertz mirrors: A key element for future terahertz communication systems," *Applied Physics Letters*, vol. 88, no. 20, p. 202905, 2006.
- [20] R. J. Williams, "Frequency Selective Terahertz Retroreflectors," MS Thesis, Department of Physics and Applied Physics, University of Massachusetts, Lowell, MA, 2014.
- [21] Lucent, Glowing-retroreflector-web.jpg, Ed., ed: Lucent Optics, 2018.
- [22] S. Rowe, "Retroreflectors: Common uses, uncommon applications and the Lunar Laser Ranging Experiment," ed. Oak Ridge, NJ: Esco Optics, 2017.
- [23] D. Desai, W. Cole, J. DeLong, and W. Zacherl, "Target Discrimination with a Laser Interrogation," in *Directed Energy Systems Symposium*, Monterey, CA, 2010.
- [24] D. Bird, "Design and Manufacture of a Low-Profile Radar Retro-Reflector," in *NATO RTO SCI Symposium on Sensors and Sensor Denial by*



*Camouflage, Concealment and Deception (RTO-MP-SCI-145)*, Brussels, Belgium, 2004, pp. 7-1 - 7-12.

- [25] L. C. Van Atta, "Electromagnetic Reflector," US Patent 2,908,002, October 6, 1959.
- [26] J. A. Vitaz, A. M. Buerkle, and K. Sarabandi, "Tracking of Metallic Objects Using a Retro-Reflective Array at 26 GHz," *IEEE Transactions on Antennas and Propagation*, vol. 58, no. 11, pp. 3539-3544, November 2010.
- [27] D. Jackson, "Introduction to Microstrip Antennas," ed, 2013.
- [28] Saturn, "915MHz Patch Antenna," 915MHz\_Patch\_Antenna-big.png, Ed., ed. Orlando, FL: Saturn PCB Design, Inc., 2017.
- [29] B. Mahafza, *Radar Systems Analysis and Design Using MATLAB*. New York, NY: Chapman and Hall/CRC, 2000.
- [30] B. Saleh and M. Teich, *Fundamentals of Photonics*, 2nd ed. Hoboken, NJ: John Wiley & Sons, 2007.
- [31] M. Abegaonkar, L. Kurra, and S. K. Koul, *Printed Resonant Periodic Structures and Their Applications*. Boca Raton, UNITED KINGDOM: Chapman and Hall/CRC, 2016.
- [32] T.-L. Wu, "Chp4. Transmission Lines and Components," in *Microwave Filter Design*, ed, 2011.
- [33] COMSOL. (2016, July 21). *The Finite Element Method (FEM)*. Available: <https://www.comsol.com/multiphysics/finite-element-method>
- [34] COMSOL, RF Module User's Guide, 2017. [Online]. Available. Accessed on July 21, 2018.
- [35] D. Kerr, *Propagation of Short Radio Waves* (MIT Radio Laboratory Series). Lexington, MA: Boston Tech, 1965.
- [36] R. A. Ross, "Radar Cross Section of Rectangular Flat Plates as a Function of Aspect Angle," *IEEE Transactions on Antennas and Propagation*, vol. AP-14, no. 3, pp. 329-335, May 1966.
- [37] nScript. (2016, July 17). *SmartPump*. Available: <https://www.nscript.com/pump-options/smartpump-tm/>
- [38] Zomega, *The Terahertz Wave eBook*, Zomega, ed., 2012. [Online]. Available. Accessed on July 22, 2018.